Numerical Simulation of the Air Flow and Particulate Deposition in Emphysematous Human Acini

by

Amitvikram Dutta

B.E. Hons., BITS Pilani, 2014

A THESIS SUBMITTED IN PARTIAL FULFILLMENT OF
THE REQUIREMENTS FOR THE DEGREE OF

MASTER OF APPLIED SCIENCE

in

THE COLLEGE OF GRADUATE STUDIES

(Mechanical Engineering)

THE UNIVERSITY OF BRITISH COLUMBIA

(Okanagan Campus)

December 2016

The undersigned certify that they have read, and recommend to the College of Graduate Studies for acceptance, a thesis entitled: NUMERICAL SIMULATION OF THE AIR FLOW AND PARTICULATE DEPOSITION IN EMPHYSEMATOUS HUMAN ACINI submitted by AMITVIKRAM DUTTA in partial fulfilment of the requirements of the degree of Master of Applied Science

Dr. Joshua Brinkerhoff, Applied Science/School of Engineering

Supervisor, Professor (please print name and faculty/school above the line)

Dr. Andre Phillion, Materials Science and Engineering, McMaster University

Co-Supervisor, Professor (please print name and faculty/school above the line)

Dr. Mina Hoorfar, Applied Science/School of Engineering

Supervisory Committee Member, Professor (please print name and faculty/school above the line)

Dr. Liwei Wang, Applied Science/School of Engineering

University Examiner, Professor (please print name and faculty/school above the line)

Dr. Neil Eves, Health and Exercise Science

External Examiner, Professor (please print name and faculty/school above the line)

12/16/2016

(Date Submitted to Grad Studies)

Abstract

Emphysema, is a destructive process that leads to the permanent enlargement of air spaces within the parenchyma of the lung. Along with chronic bronchitis, emphysema forms one of the two components of Chronic Obstructive Pulmonary Disease (COPD), a serious condition that is responsible for severe limitation of expiratory airflow in its victims. The early stages of emphysema are charecterized by the destruction of tissue in the pulmonary acinus - the part of the lung airway tree responsible of gas exchange with the bloodstream. Little is known how emphysema affects airflow within the acinus especially in the early stages of the disease. In this thesis computational fluid dynamics simulations are performed of airflow in a mathematically-derived model of a section of the pulmonary acinus. The computational domain consists of two generations of the acinus with alveolar geometries approximated as closely-packed, fourteen-sided polygons. Physiologically realistic flow rates and wall motions are used to capture the acinar flow during the inspiratory and expiratory phases of the breathing cycle. The effects of emphysema on the airway wall motion, flow rates, and septal destruction are simulated at various stages of the disease's progression to identify the effect on the flow in the acinar region. Parametric studies are presented to independently assess the relative influence of septal destruction

and the emphysematous degradation of airway motion and flow rates. The results illustrate that septal destruction lowers the flow resistance through the alveolar ducts but has little influence on the mass transport of oxygen into the alveoli. Septal destruction has a net effect on the flow field by favouring the development of recirculatory flow patterns in individual alveoli. The effects of the gradually advancing emphysema on the deposition of micron-sized particles in the acinus are also studied. The simulations are categorized according to particle size and the relative orientation of the gravitational vector to the incoming flow. Emphysematous destruction increases the deposition of particles in affected ducts, with the greatest increase occurring for the larger particle size when the gravity vector is oriented tangential to the incoming flow.

Preface

The work outlined in this thesis was conducted at UBC's Okanagan CFD Lab by Amitvikram Dutta under the supervision of Dr. Joshua Brinkerhoff and Dr. Andre Phillion. Frequent discussions on the physiological aspects of the simulations were conducted with Dr. Dragos Vasilescu, Dr. Tillie Hackett and Dr. James C. Hogg of the Heart and Lung Institute (HLI) in UBC Vancouver. I was responsible for designing and carrying out the simulations, while Dr. Brinkerhoff and Dr. Phillion helped with the interpretation of the results.

Portions of Chapter 2, 4 and 5 have been presented at a conference. Dutta A., Vasilescu D.M., Hogg J.C., Phillion A.B., Brinkerhoff J. (2016 June). Simulation of Airflow in Idealized Emphysematous Human Acinus.24th Annual Conference of the CFD Society of Canada, Kelowna.

Table of Contents

Thesis Committee . . . . . **ii**

Abstract . . . . . **iii**

Preface . . . . . **v**

Table of Contents . . . . . **vi**

List of Tables . . . . . **x**

List of Figures . . . . . **xi**

Acknowledgements . . . . . **xvii**

Dedication . . . . . **xviii**

Chapter 1: Introduction **1**

1.1 Motivation 1

1.2 Background 2

1.2.1 Human lung anatomy and physiology 2

1.2.2 Chronic obstructive pulmonary disease (COPD) . . . 2

1.2.3 Diagnosis of COPD 4

1.2.4 Emphysema 6
1.3 Approach 7
1.4 Overview of the thesis 9

Chapter 2: Literature Review 10

2.1 Anatomy of the human lung 10
2.1.1 Airway structure 10
2.1.2 Mechanism of pulmonary ventilation 12
2.1.3 Effects of emphysema on mechanical behavior of lung airways 14
2.1.4 The pulmonary acinus 17
2.2 Numerical simulations of alveolar airflows 20
2.2.1 Overview 20
2.2.2 Governing equations 21
2.2.3 The nature of alveolar flow 23
2.2.4 Numerical simulations of particulate transport in alveoli 26
2.3 CFD simulation of diseased acini 31
2.4 Summary 32

Chapter 3: Scope and Objectives 34

Chapter 4: Methodology 36

4.1 Computational domain 36
4.2 Boundary conditions and wall motion 38
4.3 Spatial mesh 44
4.4 Solution approach 46

4.4.1 Continuity and momentum equations 46
4.4.2 Finite volume method 46
4.4.3 Scalar transport 50
4.4.4 Particle transport 53
4.4.5 Initial conditions 54
4.4.6 Solution hardware 54

Chapter 5: Results and Discussion 55
5.1 Overview 55
5.2 Flow field and oxygen transport 55
5.2.1 Oxygen transport 55
5.2.2 Hydraulic losses 57
5.2.3 Flow field visualization 66
5.3 Particle transport 71
5.3.1 Simulation conditions and boundary conditions 71
5.3.2 Temporal variation of deposition fraction 72
5.3.3 Variation of steady state deposition fraction 79

Chapter 6: Summary and Conclusions 85
6.1 Model development 85
6.2 Oxygen transport and flow-field 86
6.3 Particle transport 87
6.4 Summary of conclusions 89
6.5 Future work 90

Bibliography 91

Appendix 102

List of Tables

Table 4.1 Variation of parameters governing flow-rate and air-flow motion due to emphysema 40

Table 4.2 Mesh independence study, with the observed variable being the static pressure drop across Duct I 45

Table 5.1 Simulation matrix for particle deposition study 72

List of Figures

Figure 1.1 The pulmonary airways. Adapted with permission from [1]. 3

Figure 1.2 Spirometer 5

Figure 1.3 Destruction of acinar parenchyma in emphysema. (Reproduced with permission from [2], Copyright Massachusetts Medical Society) 7

Figure 2.1 The pulmonary airways. Adapted with permission from [1]. 11

Figure 2.2 The pulmonary acinus. Adapted with permission from [3]. 12

Figure 2.3 Mechanical analogy of airways in human lung. Adapted with permission from [4]. 13

Figure 2.4 Effect of COPD on FEV_1 and FVC (Image reproduced with permission from HSE Digital Communications) 15

Figure 2.5 Variation of Flow Rate vs Volume for healthy and COPD afflicted lungs (adapted with permission from [5]) 16

Figure 2.6 Detailed cutaway of pulmonary acinus (Shared under Creative Commons Attribution 2.5 Generic license.) . 18

Figure 2.7 Alveolar shapes proposed by Weibel (Adapted with permission from [6]) 19

Figure 2.8 SEM image of terminal alveolar regions showing a close-packed honeycomb-like structure (Adapted with permission from [3]) 19

Figure 2.9 Close packed acinar geometry developed by Fung (Adapted with permission from [7]) 21

Figure 2.10 'Seperatrix' in alveolar flow (Adapted with permission from [8]) 24

Figure 2.11 Recirculatory flow in the pulmonary alveolus (Adapted with permission from [9]) 25

Figure 2.12 Relative streamlines showing the flow- field differences in proximal, medial and distal generations of the acinus (Adapted with permission from [10]) . . . 26

Figure 2.13 Deposition patterns of 3μm particle trajectories under gravity, coloured by velocity magnitude (m/s) (Adapted with permission from [11]) 29

Figure 2.14 Particle deposition efficiencies under differing gravitational orientations (Adapted with permission from [11]) 30

Figure 4.1 Computational domain of section of pulmonary acinus for present study. The blue and yellow arrows indicate the flow direction during inspiration and expiration, respectively. 37

Figure 4.2 Progressive destruction of alveolar septa in the computational domain. (a) Healthy case (b) Case I (c) Case II (d) Case III. 38

Figure 4.3 (a) Displacement of the airway wall from rest during inspiriation and expiration for the healthy and diseased cases. (b) Temporal variation of flow rate into the pulmonary acinus during inspiration and expiration for the healthy and diseased cases. 42

Figure 4.4 Computational mesh composed of tetrahedral elements. Note refined areas at inlet and outlet 45

Figure 4.5 Solution Algorithm 51

Figure 5.1 Temporal variation of the percentage increase in oxygen concentration within a duct ($\overline{C}$) for cases with both septal destruction and emphysematous wall motion/inlet flow rates. 58

Figure 5.2 Temporal variation of the percentage increase in oxygen concentration within a duct ($\overline{C}$) for cases with only emphysematous septal destruction. 59

Figure 5.3 Temporal variation of the percentage increase in oxygen concentration within a duct ($\overline{C}$) for cases with only emphysematous wall motion/inlet flow rates. . . 60

Figure 5.4 Temporal variation in the static pressure drop across the alveolar ducts for cases with both septal destruction and emphysematous wall motion/inlet flow rates. 62

Figure 5.5 Temporal variation in the static pressure drop across the alveolar ducts for cases with only emphysematous septal destruction. 63

Figure 5.6 Temporal variation in the static pressure drop across the alveolar ducts for cases with only emphysematous wall motion/inlet flow rates. 64

Figure 5.7 Velocity contours at peak inspiration (a) Healthy case (b) Case I (c) Case II (d) Case III. Arrows indicate general flow direction in the acinus. 67

Figure 5.8 Velocity contours at peak expiration (a) Healthy case (b) Case I (c) Case II (d) Case III. Arrows indicate general flow direction in the acinus. 68

Figure 5.9 Streamlines in an individual alveolus from Duct 1 near the end of inspiration for the healthy and diseased cases. Streamlines are coloured according to velocity magnitude. 69

Figure 5.10 Orientation of the gravity vector with respect to the computational geometry for the normal and tangential cases respectively 73

Figure 5.11 Deposition fraction of 1 μm particles, with the gravity vector oriented in the normal direction 74

Figure 5.12 Deposition fraction of 3 μm particles, with the gravity vector oriented in the normal direction 75

Figure 5.13 Deposition fraction of 1 μm particles, with the gravity vector oriented in the tangential direction 76

Figure 5.14 Deposition fraction of 3 μm particles, with the gravity vector oriented in the tangential direction 77

Figure 5.15 Particle deposition efficiencies under differing gravitational orientations (Adapted with permission from [11]) 78

Figure 5.16 Plot of final deposition fraction after five breath cycles for 1 μm particles, gravity vector in normal direction. The filled circles indicate healthy acinar duct while empty circles indicate emphysematous destruction. The labels indicate the duct number. 80

Figure 5.17 Plot of final deposition fraction after five breath cycles for 3 μm particles, gravity vector in normal direction. The filled circles indicate healthy acinar duct while empty circles indicate emphysematous destruction. labels indicate the duct number. 82

Figure 5.18 Plot of final deposition fraction after five breath cycles for 1 μm particles, gravity vector in tangential direction. The filled circles indicate healthy acinar duct while empty circles indicate emphysematous destruction. labels indicate the duct number. 83

Figure 5.19 Plot of final deposition fraction after five breath cycles for 3 μm particles, gravity vector in tangential direction. The filled circles indicate healthy acinar duct while empty circles indicate emphysematous destruction. labels indicate the duct number. 84

Acknowledgements

First and foremost I would like to gratefully acknowledge the guidance and help provided by my principal supervisor, Dr. Joshua Brinkerhoff. No less important was the direction provided by Dr. Andre Phillion, who defined the extent of the thesis.

I would also like to acknowledge the help provided to me by Dr.James C. Hogg, Dr. Dragos Vasilescu and Dr. Tillie Hackett of the the Heart and Lung Institute in Vancouver, for providing necessary and valuable insight into the nature of COPD.

My colleagues and friends at the Okanagan CFD Lab have provided invaluable assistance in the form of ideas and feedback and this thesis could have been borne to fruition without their help. I would also like to acknowledge other colleagues and friends at the School of Engineering at UBC Okanagan, particularly Mr. Oleg Shabarchin.

Dedication

To my parents, for the start they gave me in life.

Chapter 1

Introduction

1.1 Motivation

This thesis studies the effects of early onset emphysema in human lungs by means of numerical simulation of the airflow in diseased and healthy portions of the lungs. Emphysema is one of the component conditions of Chronic obstructive pulmonary disease (COPD), which is defined as "... a persistent airflow limitation that is usually progressive and associated with enhanced chronic inflammatory response within the lung to noxious particles or gases" [12]. Thus COPD is an umbrella term for a host of conditions which may produce the symptoms that are outlined in its definition.

COPD is projected to become the third leading cause of death worldwide by 2020 [12]. In addition to direct economic costs associated with the treatment of the disease (estimated to be $1.5 billion per year in Canada alone [13]), COPD also has significant impacts on quality of life and productivity in the workplace [12]. Clearly, a deeper understanding of the components of this disease, its genesis, progression and its attendant effects is of the essence.

1.2 Background

1.2.1 Human lung anatomy and physiology

The human lungs are a pair of air-filled organs that are primarily responsible for gas-exchange between the atmosphere and the bloodstream. Air is transported into each lung through a network of dichotomously branching airways which branch off from the trachea which is the primary airway and these airways decrease in diameter with each distal generation. The airways are divided into two distinct generations, the conducting and respiratory airways. The former transports the air into the respiratory zone which is responsible for the gas-exchange process. While the conducting airways are smooth walled, the respiratory zone has airways whose walls are populated with structures known as known as alveoli. These walls of these alveoli are thin enough to permit diffusive exchange of gases between the lung air and the blood-stream thereby supplying fresh oxygen while carrying away carbon-dioxide.

1.2.2 Chronic obstructive pulmonary disease (COPD)

The chronic airflow limitation in COPD is caused by two specific syndromes: emphysema and small airways disease (obstructive bronchiolitis) [12]. Emphysema is the deterioration of pulmonary tissue, called parenchyma, and it results in loss of respiratory airways for gas exchange and elastic recoil. Small Airways Disease affects airways of diameters less than 2 mm and causes structural changes including remodelling and narrowing. Chronic bronchitis is also frequently included as one of the component entities of

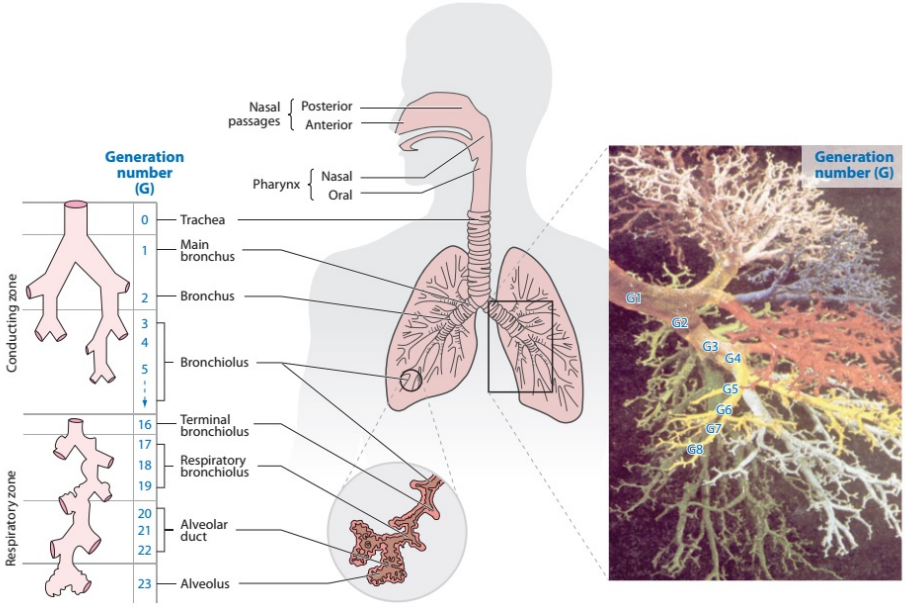

Figure 1.1: The pulmonary airways. Adapted with permission from [1].

COPD [12, 14]. It is defined as "...the presence of cough and sputum production for at least three months of two successive years" [12]. However, chronic bronchitis may exist independently of the airflow limitation, considered to be the defining feature of COPD [15], and is thus not considered in the present study. The extent of contribution of emphysema, small airways disease and chronic bronchitis and indeed their presence is highly variable within the population of COPD patients. Thus, in some cases, emphysema accounts for a significant part of the airflow limitation, while in other instances it might only play a secondary role. Additionally, COPD often co-exists with other diseases, which may complicate its diagnosis [12].

The most well-known risk factor for COPD is inhaled cigarette smoke with the amount of and duration of smoking contributing directly to the rela-

tive severity of the disease [12]. However, there is evidence that non-smokers may also develop chronic airflow limitation, and among people with the same smoking history, not all will develop COPD [12]. Globally, COPD has also been linked to sustained exposure to combustion products of biomass fuels such as coal, wood and straw [16], and inhalation of organic and inorganic dusts, chemical agents and fumes [17]. Additional factors, including genetics, gender, age, lung growth, socio-economic status and childhood infections have also been acknowledged as having a role in the progression of this disease [12, 16]. The most well established genetic risk factor is the deficiency of alpha—1 antitrypsin. This serum acts as an inhibitor and is released during lung inflammation in order to protect the body from harmful effects of other enzymes [18].

1.2.3 Diagnosis of COPD

The three primary symptoms of COPD are chronic cough, breathlessness and sputum production. Tightness of the chest and wheezing sounds may also be present [12]. A diagnosis of COPD is usually considered for any patient that displays these three characteristic symptoms. However, clinical diagnosis is only made after performing a Lung Function Test (LFT) [12, 19]. This operation is carried out in two identical parts, before and after administration of an inhaled bronchodilator. Specifically, the patient is asked to take in a full breath and then exhale the air in a forced manner until the lungs are emptied and with the aid of a recording device known as a spirometer (Fig. 1.2), two parameters are measured. The Forced Expiratory Volume in one second (FEV_1) is the volume of air exhaled in the first sec-

ond, while the Forced Vital Capacity (FVC) is the total volume of air that can be exhaled with no time constant. In both parts, the $((FEV_1)/FVC)$ ratio is calculated and if this value is less than 0.7 after the inhalation of the bronchodilator, then a diagnosis of COPD is usually considered [12].

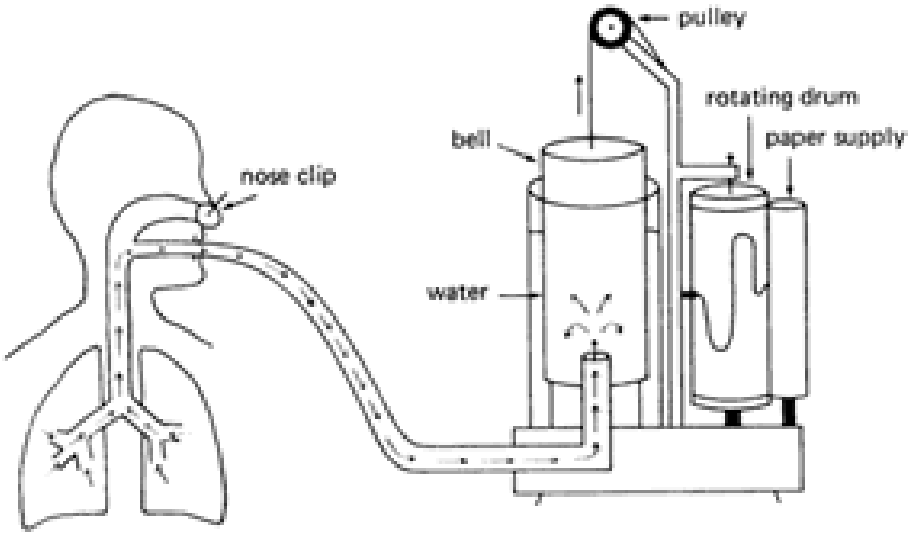

Figure 1.2: Spirometer

Studies have shown that early detection and treatment of COPD yields substantially better results for patients [12, 20]. However, the early detection of COPD is problematic, since in a majority of the cases patients are either asymptomatic or attribute the early symptoms of COPD, such as increasing lack of breath, to advancing age [20]. Airway conditions in the lower airways are also difficult to diagnose [21] with the standard lung function tests and spirometry. This results in many patients being diagnosed only after considerable and irreversible damage has occurred to the lungs. Additionally, commonly published spirometry data has significant discor-

dance amongst various references [22] and the American Thoracic Society has recommended against using spirometric parameters to diagnose lower airway disease [23]. Therefore, there exists a gap in understanding within the medical community of the effects of the progression of emphysematous destruction in the earliest stages of COPD, which in turn hinders access to possible routes towards early diagnosis. While it has been confirmed that the earliest stages of emphysema are characterised by the destruction of airways in the pulmonary acinus, the effects of their destruction on the airflow and particle deposition in the alveolar spaces are unknown. In addition, while this destruction has been correlated to the increase in resistance to airflow, the effects of this decreased airflow and indeed the effects of the progressive nature of the destruction have yet to be quantified.

1.2.4 Emphysema

The word emphysema originated from the Greek term "*emphysan*" , meaning "blow into" [24]. When applied to the lungs, it implies excessive air within the parenchymal tissue of the lung [24]. The definition of emphysema as it stands today originated in a 1984 workshop held by the Division of Lung Disease at the National Heart and Blood Institute, which stated that emphysema is "... a condition of the lung, characterized by abnormal, permanent enlargement of air-spaces, distal to the terminal bronchiole, accompanied by destruction of their walls and without obvious fibrosis" [25, 26].

The emphysematous condition of the lung is characterized by loss of alveolar walls, as depicted in Fig. 1.3, which in the case of closely packed

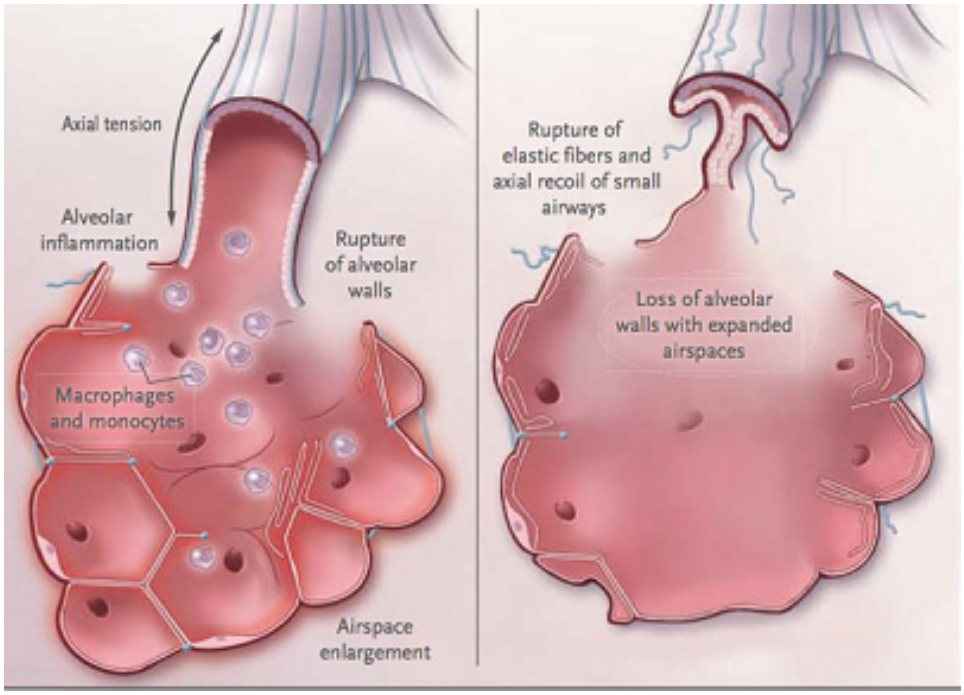

Figure 1.3: Destruction of acinar parenchyma in emphysema. (Reproduced with permission from [2], Copyright Massachusetts Medical Society)

lower generations of the acinus also forms the with subsequent destruction of the capillary bed. The air-spaces are dilated and the small airways are narrowed and have atrophied walls [5]. This implies that pulmonary airways lose their connection with the inner surface of the lung, which hitherto had been provided by the elastic parenchymal mesh.

1.3 Approach

Traditional experimental methods of direct observations on the effects of this disease are not applicable for the study of early stage COPD. With Computed Tomography (CT), airways are only visible for approximately 6

or 7 generations, while the airways which form the pulmonary acinus are usually below the resolution of conventional CT [27]. Magnetic Resonance Imaging (MRI), which is also frequently used for pulmonary diagnostics is hampered by a low signal return due to lack of tissue in the alveolar spaces. This is further excarbated in emphysema due to loss of tissue [28]. As a result, while excised lung tissue from deceased human subjects may later be studied *ex vivo* under high resolution micro-CT studies, the same cannot be said for living tissue under *in vivo* conditions. This shortcoming in the experimental method is hereby overcome by the use of numerical simulation.

A simulation-based approach is also justified due to the ability to artificially control the conditions of the simulation by the modeller. This allows for identifying the relative importance of various effects that cannot be independently controlled in a laboratory setting. Not only does Computational Fluid Dynamics (CFD) simulation allow observation of the effects of the disease on the airflow, but it also allows the progressive nature of the disease to be modelled with a greater degree of control than can be obtained from *ex vivo* samples. Additionally CFD simulation techniques allow real-time values of variables such as particle deposition to be simulated under a variety of controlled conditions that would be extremely hard to replicate under experimental conditions.

This thesis studies the effects of destruction of parenchymal tissue in the acinar airways due to emphysema by building a model which incorporates the effects of the disease on the airway wall motion and airflow in the pulmonary acinus. Specifically, numerical simulations of the airflow are then carried out in order to determine the effects of the disease, the severity of

which is progressively increased over successive iterations. The results of these simulations are then subsequently used to determine consequences of the progressive nature of the disease on oxygen transport, pressure drop in the alveolar ducts and particle deposition in the pulmonary acinus.

1.4 Overview of the thesis

The remainder of the thesis is divided into five parts. Chapter 2 includes a detailed literature review covering COPD in general, emphysema in particular, and CFD approaches that have been employed to date in order to simulate airflow in the human lungs. This is followed by a detailed explanation of the scope and objectives of the thesis in Chapter 3. Chapter 4 details the numerical methods that have been employed in the study, followed by the results and their discussions in Chapter 5. A summary of the thesis, its conclusions, and recommended future work is given in Chapter 6.

Chapter 2

Literature Review

2.1 Anatomy of the human lung

2.1.1 Airway structure

The root of the human airway tree is the trachea or windpipe. This structure, which measures 1-2 cm in diameter in normal adult human lungs [29], branches in the chest cavity with one daughter branch per lung. The left and right bronchi subsequently undergo multiple dichotomous subdivisions leading to daughter bronchioles and finally terminal bronchioles. This dichotomous branching was detailed in Fig 1.1 and is repeated in Fig 2.1.

The detailed anatomical structure of airways was first characterised through the study of preserved cadaver lung tissue [6, 30]. These studies established the dichotomous nature of the airway branching. These airways were later shown to span up to an average of 23 generations [31]. The airway generations are numbered from the trachea which is generation zero and each subsequent branching increases the generation number by one as seen in Fig 2.1. Also depicted in Fig. 2.1 is the functional classification of the pulmonary airway system. The airways may be broadly divided into two regions. The first region -the conducting airways- has the trachea as its

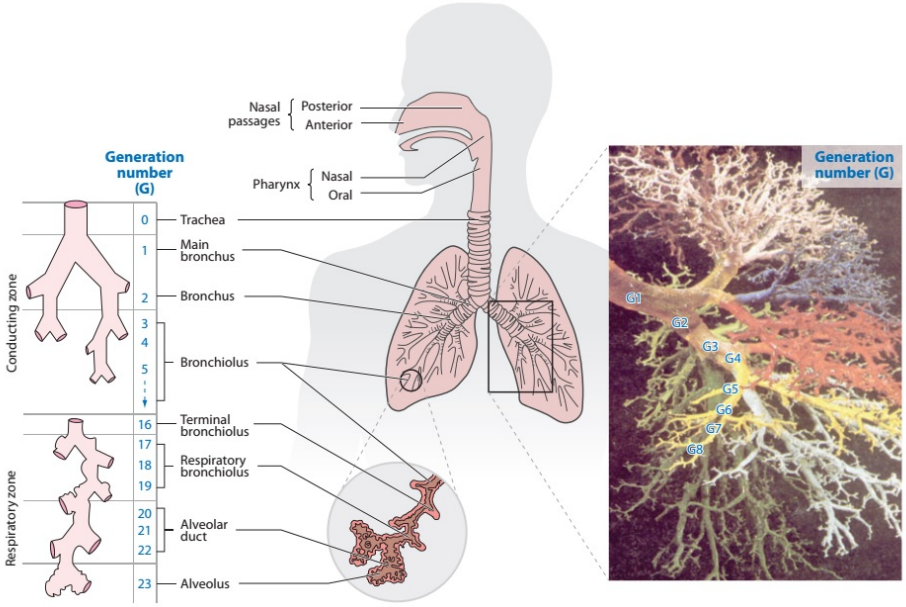

Figure 2.1: The pulmonary airways. Adapted with permission from [1].

root and consists of smooth-walled airways whose sole function is to conduct the flow deeper into the lung [6]. This region spans approximately 14 generations of dichotomous branching. The final bronchioles of this generation are termed as the terminal bronchioles. The subsequent generations -the respiratory airways- comprise the respiratory zone. From herein, as the flow descends, the walls of the airways begin to be populated by individual, isolated structures known as alveoli. These transitional bronchioles with isolated alveoli form the beginning of the respiratory unit known as the pulmonary acinus. The acinus represents the basic unit responsible for exchange of gases between the bloodstream and the lung. The alveoli continue to increase in size among the more distal airways [32] until finally they cover the entire surface of the airway with each alveolus having an opening into

the common duct [33]. Fig. 2.2 depicts a single pulmonary acinus spanning eight generations; the respiratory bronchioles showonly isolated alveoli while alveolar ducts are completely covered with alveolar outgrowths.

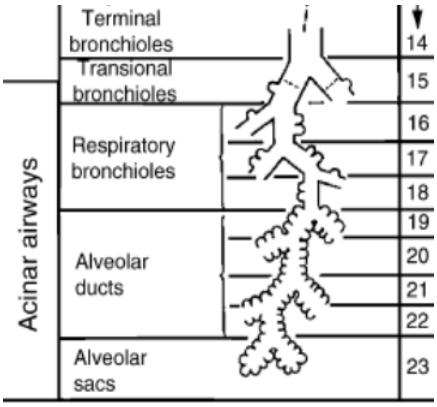

Figure 2.2: The pulmonary acinus. Adapted with permission from [3].

2.1.2 Mechanism of pulmonary ventilation

The physiological function of pulmonary ventilation — or what is more commonly known as the act of breathing — is to ensure a gas exchange that meets the requirements of tissue metabolism in the body, thereby ensuring homeostasis [34]. This requires airflow through the pulmonary airways, to the alveoli, which are the sites of gas exchange. The presence of such a flow may be achieved by creating a pressure difference between the two ends of the airways. Therefore, during inspiration, the pressure in the airways must be lower than the ambient pressure at the mouth and vice versa during expiration.

Inspiration is an active process, whereby the contraction of the diaphragm and the external intercostal muscles expand the tissue matrix, inflating the

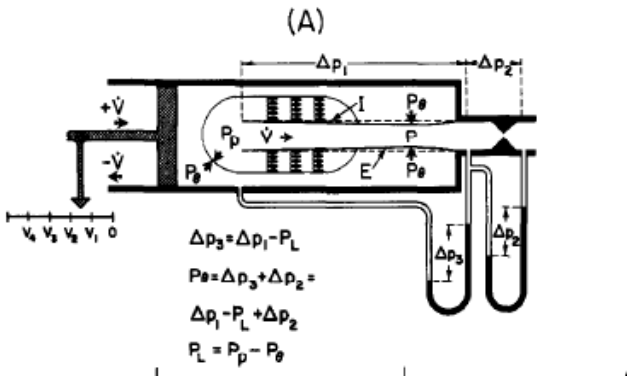

Figure 2.3: Mechanical analogy of airways in human lung. Adapted with permission from [4].

airways and generating the suction pressure required [34]. This is illustrated in Fig. 2.3 where the springs attached to the tube representing the airway mimic the action of the elastic tissue matrix during the breath cycle. As the air flows into the lungs, the pressure equalises with the atmosphere, until there is no more flow, which signals the end of inspiration. Normal or tidal exhalation by contrast is a passive process. As the intercostal muscles relax, the natural elasticity of the parenchymal tissue recoils the fibres attached to the airways thereby compressing them. This phenomenon, known as elastic recoil, is responsible for compressing the airways, increasing the pressure in them, and driving the air out.

2.1.3 Effects of emphysema on mechanical behavior of lung airways

The primary effect of emphysema on the mechanics of the lung is the loss of elastic recoil. This in turn reduces the expiratory driving pressure [35]. This translates to a reduced airflow during expiration in a condition that is termed as Expiratory Flow Limitation (EFL). Under EFL conditions the expiratory flow rate becomes independent of expiratory muscle effort. Instead the flow rate is determined by the static lung recoil pressure and resistance of the airways up-stream from the affected segments [36, 37]. The EFL conditions also increase the time required for a complete expiration of the air inhaled during the inspiratory phase. This fact coupled with the loss of elastic recoil directly leads to an increase in the End-Expiratory-Lung Volume (EELV)- the residual volume of the lung at the end of expiration [35]. This is in turn quantified by the variable forced vital capacity (FVC). FVC is defined as the amount of air which can be forcibly exhaled from the lungs after taking the deepest breath possible. This can be measured using spirometric techniques discussed in Chapter 1 and as depicted in Fig 2.4 COPD also results in a decrease in FVC. This is directly linked to the loss of elastic recoil [5] and results in air-trapping in the lung. This adds to the permanent enlargement of the air-spaces, parts of which had been previously rendered void, by the loss of parenchymal tissue.

As a result the expiratory flow is limited and significantly hampered. Additionally, during inspiration the maximum flow rate is observed to decrease in patients with emphysema. As a result, both during inspiration and expi-

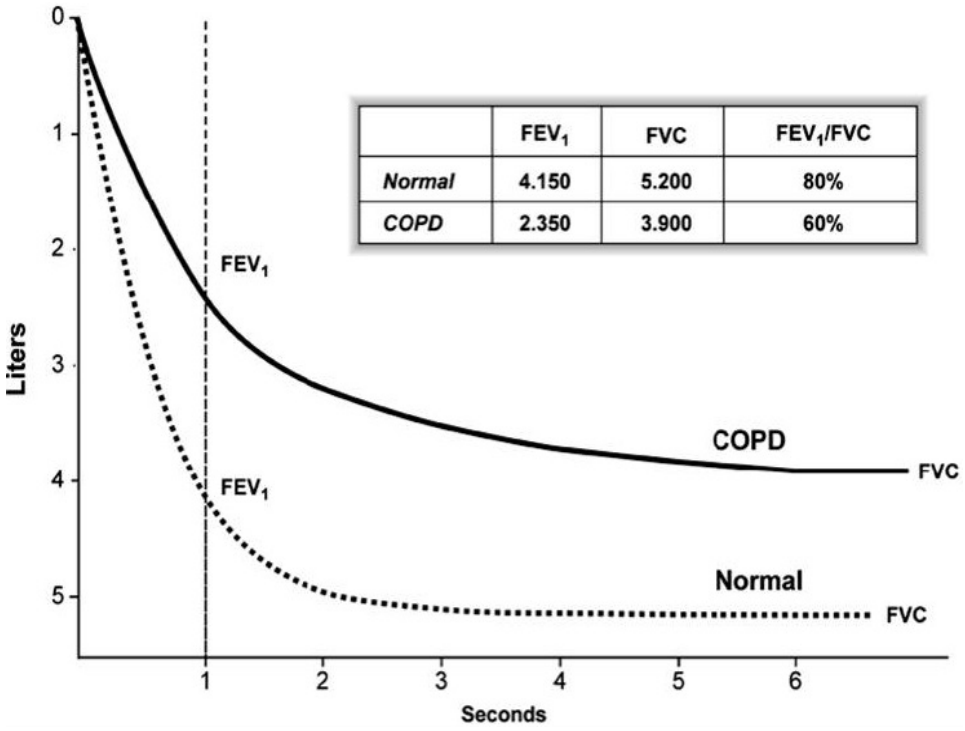

Figure 2.4: Effect of COPD on FEV_1 and FVC (Image reproduced with permission from HSE Digital Communications)

ration the natural self-similar motion of the alveolar airways is truncated and as a direct consequence the magnitude of airflow through them, decreases.

The classic description of how the flow rate of air in and out of the lungs varies with volume is given in Fig. 2.5. During inspiration, the flow rate dependence on volume is appreciably sinusoidal (COA). During expiration, the flow rate rises with decreasing volume linearly (OB), until it reaches a maximum expiratory flow rate (B). Thereafter it falls to zero linearly (BC), signalling the end of complete expiration. The values of the corresponding quantities for a patient suffering from COPD are shown in red on the same

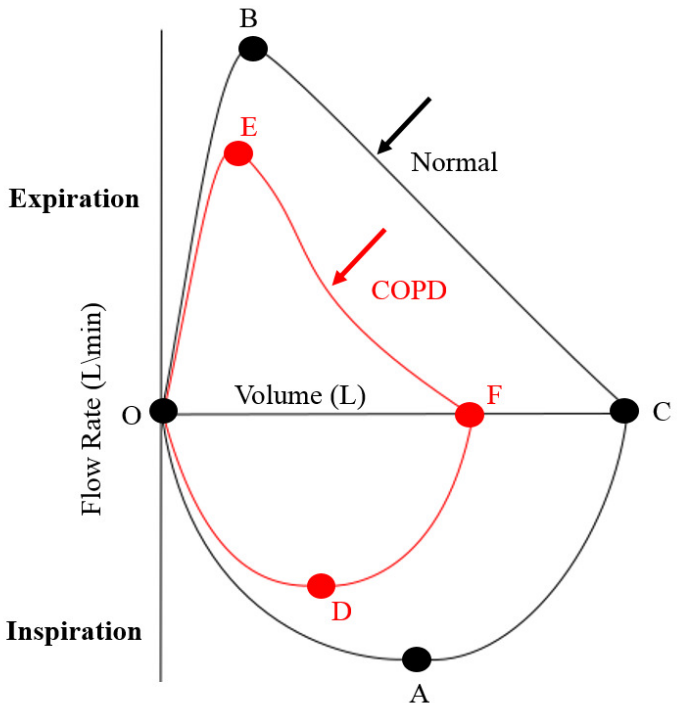

Figure 2.5: Variation of Flow Rate vs Volume for healthy and COPD afflicted lungs (adapted with permission from [5])

figure. As mentioned before the maximum flow rate during inspiration and expiration for the diseased case (D and E respectively) is reduced, when compared to the healthy case.

Although these values in Fig. 2.5 reflect the variation of the whole lung volume and the flow rate measured at the mouth, it is assumed they would reflect the volume flow rate relationship in an alveolar duct. It is also important to note that the volume values plotted on the horizontal axis do not represent the actual volume of the lung or alveolus itself, but rather, the variation in volume from the resting position prior to inspiration as is represented by points O and C in Fig 2.5.

2.1.4 The pulmonary acinus

The dichotomously branching airways of the pulmonary airway tree terminate in structures that are termed as acini. The pulmonary acinus forms the respiratory zone of the airway tree and is termed as such since it is the principal location of gas exchange between the inhaled air and blood vessels. This complexity of structures necessary to achieve efficient gas-exchange is detailed in Fig 2.6. The velocity of airflow in these airways is much lower than that of the higher conducting airways and this serves to promote the diffusive exchange of gases.

The geometrical shape of the alveoli is a matter of some debate. The seminal work by Weibel [6] mentions three distinct possibilities based on surface-area and volumetric measurements. Two are trapezoids with the third being a spherical cap as shown in Fig. 2.7. In recent years the model of the spherical cap with parameters established by [32] has been popular

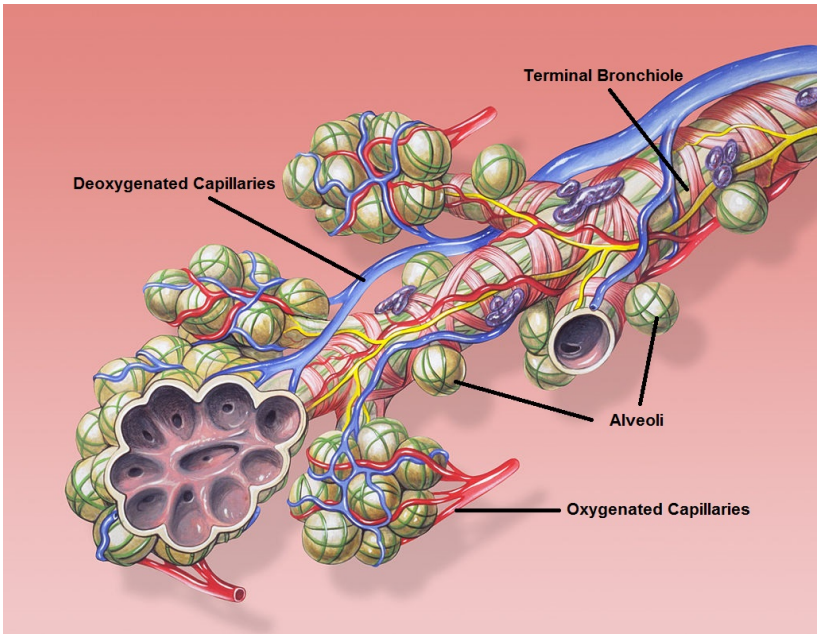

Figure 2.6: Detailed cutaway of pulmonary acinus (Shared under Creative Commons Attribution 2.5 Generic license.)

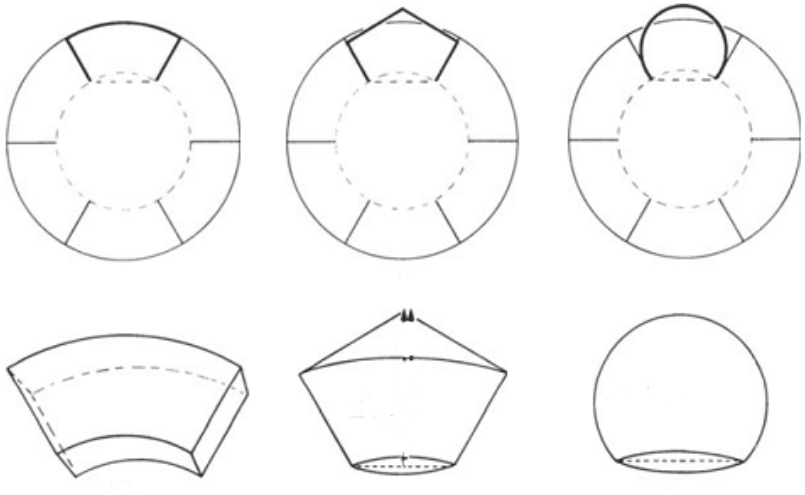

Figure 2.7: Alveolar shapes proposed by Weibel (Adapted with permission from [6])

in studies relating to flow in the respiratory zone [9, 38, 39]. However, this geometry has a number of shortcomings. In particular, it does not represent the close packed nature of the alveoli that is usually observed in the terminal regions of the respiratory zone (Fig. 2.8). In order to address

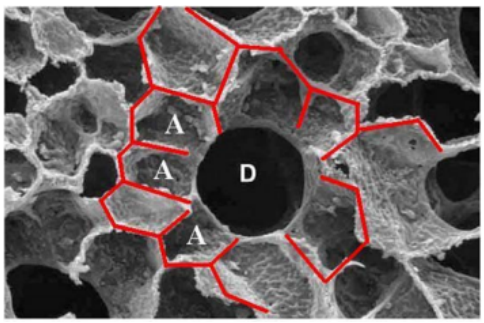

Figure 2.8: SEM image of terminal alveolar regions showing a close-packed honeycomb-like structure (Adapted with permission from [3])

the shortcomings of the alveolar cap models, an alternative arrangement of

alveoli in the acinar regions was proposed by Fung [7]. The proposed model was envisaged on the basis of three assumptions; 1) all alveoli are equal and space-filling before they are ventilated, 2) they are ventilated to ducts as uniformly as possible, 3) the alveoli are reinforced at their mouths for structural integrity. In this model the basic unit of the acinus is a truncated 14-hedron, henceforth termed as an order 1 polyhedron (Fig. 2.9a). A single 14-hedron, surrounded by identical polyhedra on each of its faces forms a single solid unit in space (Fig. 2.9b), henceforth termed as an order 2, 14-hedron. This forms a basic unit of the acinar-structure. A combination of order-2 and order-1 polyhedra can then be assembled into a ductal tree forming a space-filling structure (Fig. 2.9b.). The structures formed by close-packing alveoli of this shape resemble honeycombs and have featured in recent works which have tried to accurately depict the space-filling nature of the alveoli [8, 11]. The fact that the geometrical structure of the alveoli is significant enough to influence properties such as deposition of particles [40, 41] requires that the choice of any geometry for a particular simulation be accompanied by proper justification.

2.2 Numerical simulations of alveolar airflows

2.2.1 Overview

The airways of the lung present a complex environment in where low velocity flow transports gases through both convective and diffusive means. While the geometries may be approximated to some degree as cylindrical structures, the dichotomous branching of the upper lung and the presence of

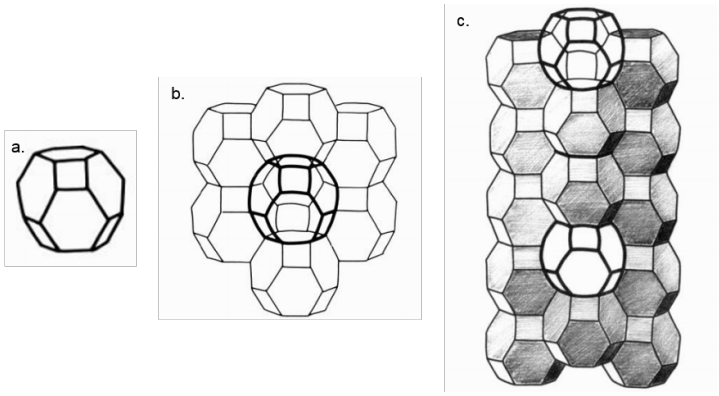

Figure 2.9: Close packed acinar geometry developed by Fung (Adapted with permission from [7])

alveolar openings in the respiratory zone make for a complex environment. Consequently, computational fluid dynamics (CFD) simulations have been used to gain additional insights into the flow structures during inhalation and exhalation. This section reviews the mathematical background of CFD simulations and focuses specifically on its use for simulating alveolar flow.

2.2.2 Governing equations

Respiratory air-flows are generally considered to be examples of Newtonian and incompressible flows[1, 42]. They are therefore, described by the Navier-Stokes equations in a dimensionless form as given in [43].

$$(Wo)^2 \frac{\partial u^*}{\partial t^*} + Re(u^* \cdot \nabla^*)u^* = -\nabla^* p^* + \nabla^{*2} u^* \tag{2.1}$$

where:

$$\nabla^* = D\nabla,\ t^* = \omega t,\ u^* = \frac{u}{U},\ p^* = \frac{p}{\mu U/D}$$

with u being the velocity field, p is the pressure, t is the time, ρ is the density, D is the airway diameter, μ is the molecular viscosity, and $\omega = (2\pi/T)$ is the angular frequency of the breathing time period T.

Two particular dimensionless numbers are important in the context of the given equations. The Reynolds number given by

$$Re = \frac{\rho U D}{\mu}$$

represents the relative influence of the inertial forces and viscous forces on the fluid flow. In pulmonary airflows during quiet sedentary breathing, Re is $O(1)$ or smaller [43], therefore the inertial forces are generally negligible and the flow in the acini is laminar. Due to the cyclic nature of the flow in the pulmonary airways, a second dimensionless number is required to characterize this unsteadiness. This is the Womersley number,

$$Wo = D(\frac{\omega U}{\mu})^{0.5}$$

which compares unsteady acceleration to viscous effects. For typical acinar flows, Wo is $O(0.1)$ [43]. This implies the frequency of airflow cycles is sufficiently low that a parabolic velocity profile has time to develop during each cycle. The dichotomous branching nature of the airway tree lends itself to a straightforward computation of the airflow rate in the z^{th} generation of the tree as

$$U(z) = 4Q/(2^z \pi D(z)) \tag{2.2}$$

where Q is the flow rate at the trachea ($z = 0$) and $D(z)$ is the diameter of

the airways in the z^{th} generation. However, it is important to note that this relation is only valid for ideal cylindrical airways and identical diameters at any given generation. In the conducting region, the diameters of the airways conform to theoretical predictions [44], and thus the velocities conform to Eqn. 2.2. In the acinus, however, the effective diameters are larger [32], and velocities tend to decay more steeply. It should also be noted that Eqn. 2.2 is only valid if the longitudinal paths to all airways in a particular generation are assumed to be identical. Even though the transpulmonary pressure across the airways may be assumed to be homogeneous throughout the lung, the airways themselves may be of different longitudinal lengths. As a result, for a constant pressure drop ΔP, an airway with a longer longitudinal path to the terminal alveolar sacs will have higher viscous resistance, and thus lead to an airway with a lower flow rate despite sharing the same diameter as its neighbor of the same generation with a shorter longitudinal path [43].

2.2.3 The nature of alveolar flow

To the best of the author's knowledge, the earliest numerical analysis of flow in the acinus was an investigation of creeping flows by the method of solving the bi-harmonic equation for the stream-function [45]. Studies of flow in packed acini followed thereafter [46, 47]. Simulation of flows in the alveolar domain has been primarily motivated by the need to study how aerosols and other fine particles behave in this regime [40, 48, 49]. To this end, investigations have shown that the orientation of the branching alveolar ducts with respect to each other as well as to the gravity vector are important in determining deposition sites of micro-particles [49, 50].

The alveolar topology makes alveolar flows resemble a ductal shear layer passing over a cavity formed by the opening of the alveolar mouth. This is illustrated in Fig. 2.10. Such an arrangement can give rise to flow separation and formation of a recirculation zone, depending on geometrical and flow parameters. In the flow regime encountered in the acinar region, the relative arrangement of the duct and cavity determines the occurrence and nature of flow-separation, particularly the location of the separation surface or 'seperatrix' [8, 51].

Incorporating wall-motion into the simulation mimics the distentions of the lung parenchyma, and is crucial in capturing the three-dimensional recirculating flow structures that are characteristic of acinar flows [39].

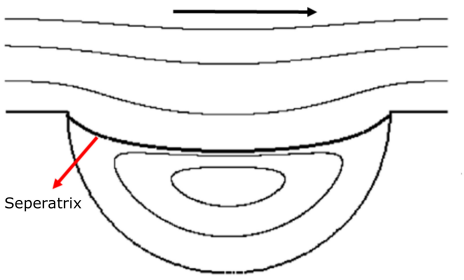

Figure 2.10: 'Seperatrix' in alveolar flow (Adapted with permission from [8])

Since alveolar flows are a result of pressure gradients arising from distension of the lung airways, the effect of airway motion on the flow is also critical. While there is evidence that rigid walled alveolar models give rise to recirculatory flows, [49, 52], wall motion kinematics into numerical simulations of acinar airflows result in flow patterns that are irreversible and chaotic in nature [9]. This phenomena is termed as chaotic advection and is frequently observed in 2D time dependent and 3D cavity flows [53, 54].

This makes the alveolar flows inherently complex. Recirculating flows cre-

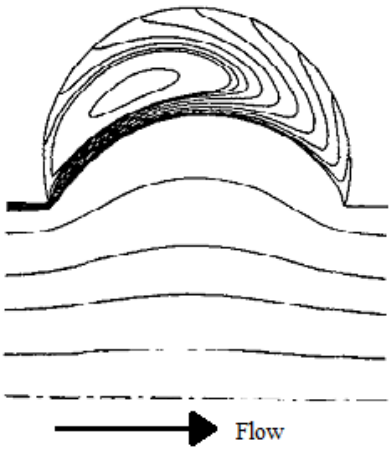

Figure 2.11: Recirculatory flow in the pulmonary alveolus (Adapted with permission from [9])

ate stagnation points that result in irreversible paths of massless particles [9, 38]. The first simulations to incorporate moving alveolar walls indicated that in realistic alveolar geometries have the stagnation point form at the proximal end of the alveolar cavity, as shown in in Fig. 2.11. Subsequent simulations incorporating 14-hedron geometries showed that the position and strength of the recirculatory centre is dependent on the location of the alveolar generation. The proximal generations have a strong recirculation centre develops at nearly the centre of the cavity. Distal generation show a weakening of the centre accompanied by a shift to the proximal end of the alveolus while the distal generation show no recirculation as shown in Fig. 2.12. The velocities within the alveolar cavities are on average one or two orders less in magnitude than in the duct [8, 39].

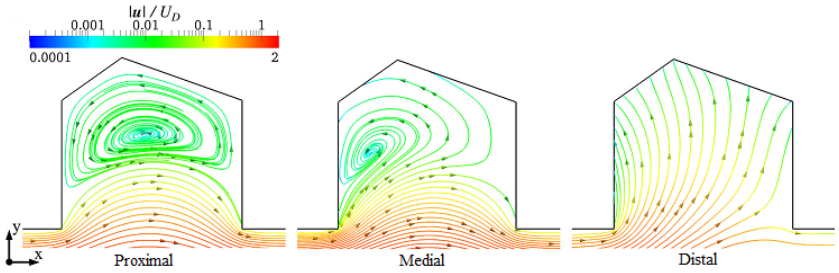

Figure 2.12: Relative streamlines showing the flow- field differences in proximal, medial and distal generations of the acinus (Adapted with permission from [10])

Under healthy conditions the nature of flow within the alveolus is heavily dependent on its location within the acinar generation. In the proximal generations a strong recirculatory zone is observed with the vortex centre close to the centre of the alveolus. In the medial generations the centre moves to the proximal end of the alveoli while in the distal generations the recirculatory centre disappears and is replaced by radial flows.[10]

2.2.4 Numerical simulations of particulate transport in alveoli

Governing equations

The transport of particles in the pulmonary acinus is described by the following equation [43]

$$m\frac{\mathrm{d}\boldsymbol{u_p}}{\mathrm{d}t} = \boldsymbol{F_D} + \boldsymbol{F_g} + \boldsymbol{F}(t) \tag{2.3}$$

Where the particle acceleration on the left hand side is a result of the three forces on the right. $\boldsymbol{F_g}$ is the gravitational force on the particle with $\boldsymbol{F_g} = m\boldsymbol{g}$. $\boldsymbol{F_D}$ is the drag force on the particle, which in the instance of a low Re flow, is given by the Stokes Law:

$$\boldsymbol{F_D} = \frac{-3\pi d_p \mu(\boldsymbol{u}_p - \boldsymbol{u}_f)}{C_c} \tag{2.4}$$

The drag force is therefore dependent on the particle diameter d_p, the fluid viscosity μ and the relative velocity of the particle $\boldsymbol{u}_p$ with respect to the entraining fluid $\boldsymbol{u}_f$. C_c is the Cunningham slip factor [55]. The third term on the right $\boldsymbol{F}(t)$, is a stochastic force representing the Brownian motion due to the collisions of the fluid molecules with the entrained particles. These three forces are representative of the three competing mechanisms that determine the fate of an inhaled particle in the acinus. Namely, convection, sedimentation and diffusion. The extent to which each of these forces dominate the particle dynamics in the pulmonary airways is a function of particle size and will be discussed in the following section.

Micron sized particle dynamics in the pulmonary acinus

For micron sized particles, where $d_p > 0.5\mu m$, the diffusive force due to the Brownian motion ceases to have a significant impact on the particle dynamics [56]. Eqn. 2.3 may then be non-dimensionalized by some characteristic velocity $\boldsymbol{u}$ and length L, as

$$Stk\frac{\mathrm{d}\boldsymbol{u}_p^*}{\mathrm{d}t^*} = -(\boldsymbol{u}_p^* - \boldsymbol{u}^*) + \frac{u_g \boldsymbol{g}^*}{\boldsymbol{u}} \tag{2.5}$$

where

$$\boldsymbol{u}_p^* = \frac{\boldsymbol{u}_p}{\boldsymbol{u}}; \quad \boldsymbol{u}_f^* = \frac{\boldsymbol{u}_f}{\boldsymbol{u}}; \quad t^* = \frac{t\boldsymbol{u}}{L}; \quad g^* = \frac{\boldsymbol{g}}{|\boldsymbol{g}|}$$

$$Stk = \frac{\rho_p d_p^2 \boldsymbol{u}}{18\mu L}$$

is the Stokes' number representing the ratio of the inertial forces to the viscous drag force,

$$\frac{u_g}{\boldsymbol{u}} = \frac{\rho_p d_p^2 |\boldsymbol{g}|}{18\mu |\boldsymbol{u}|},$$

and compares the relative effects of gravity to the viscous drag force with the terminal settling velocity given by u_g. While the inertial term is significantly more important in the conducting airways, in the acinar airways, due to the low values of Re, it is the gravity term that dominates.

It is important to note that the relative strength of the two mechanisms is highly dependent on particle sizes. Sznitman et. al. [11] investigated the particle dynamics of 1 μm and 3 μm particles in two separate geometries; namely, a simple isolated alveoli on an airway, consisting of one half-spherical alveolus and a space filling geometry of the entire acinus derived from the model developed by Fung [7].

It was observed, that while the larger 3 μm particles (as shown in Fig. 2.13) remained relatively insensitive to the flow and were governed almost entirely by the orientation of the gravitational field, the smaller particles (1 μm) exhibited complex kinematics due to the coupling of the un-

steady flow field, local convective effects due to the complex geometry of the acinus and the sedimentation effects of the gravitational field. For both particle sizes, the deposition patterns were largely non-uniform, determined primary by orientation of the gravity vector relative to the duct. Particle entry into the alveoli itself was governed largely by the position of the alveolar openings relative to the direction of sedimentation, which was the principal determinant of the particle kinematics. This also implies that in spite of the low flow velocities, under appropriate circumstances, particles may be swept deep into the acinus.

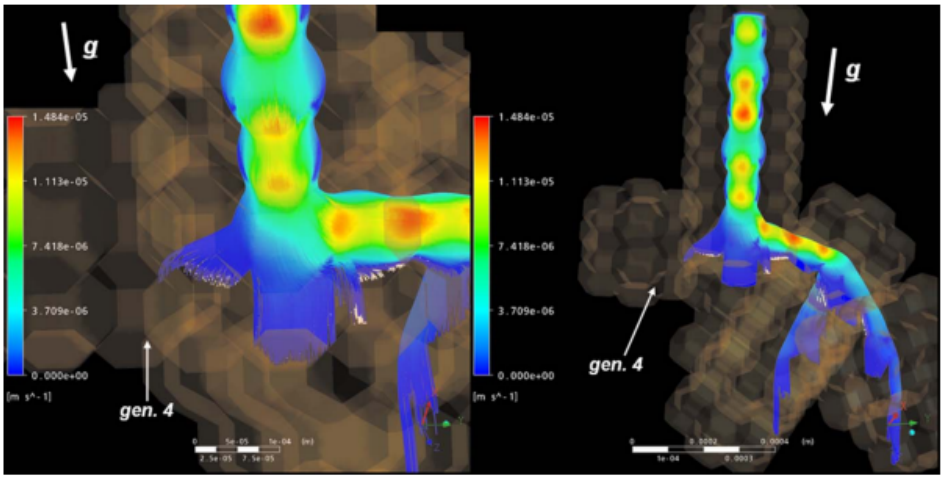

Figure 2.13: Deposition patterns of 3μm particle trajectories under gravity, coloured by velocity magnitude (m/s) (Adapted with permission from [11])

The deposition patterns of the two particle sizes was studied using the deposition efficiency, defined as the ratio of the particles inhaled to those deposited over a specified time period. It was observed that while the heavier particles (3 μm) were deposited within a single breath cycle, the finer particles (1 μm) would exhibit much longer residence times (3 times longer

than the heavier cases). As shown in Fig. 2.14, the heavier particles reach a deposition efficiency of approximately 1, within halfway of the first breath cycle ($t/T = 0.5$). In contrast the lighter particles in one case show a deposition efficiency of approximately 0.9 at ($t/T = 1.5$), while in the other case the efficiency remains slightly above 0.8 even after $t/T = 3$. This fact implies that the finer particles remain longer in suspension within the flowstream and concurs directly with their more complex coupled dynamics as discussed earlier.

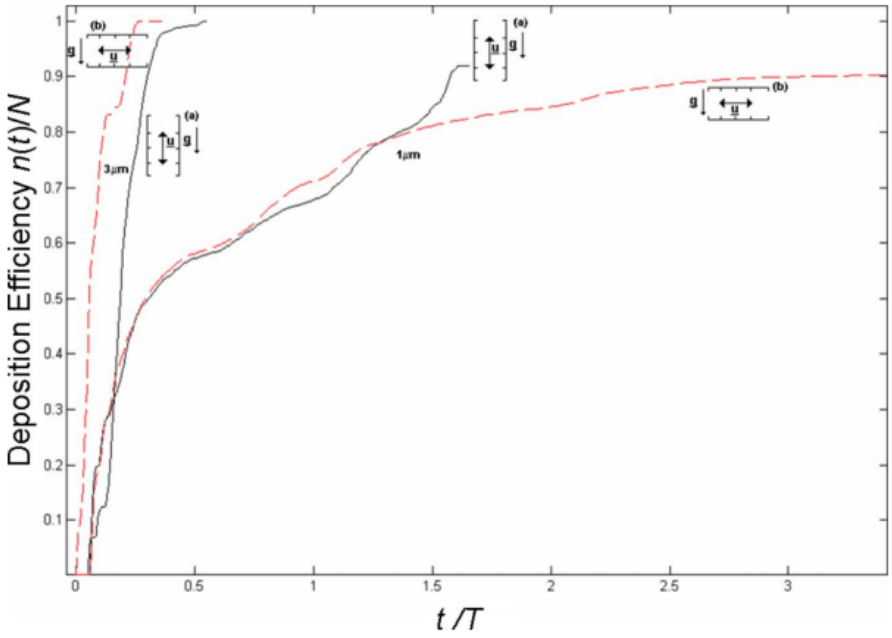

Figure 2.14: Particle deposition efficiencies under differing gravitational orientations (Adapted with permission from [11])

2.3 CFD simulation of diseased acini

The majority of the numerical studies detailed to date have dealt with undamaged alveolar geometries with flow and boundary conditions reflecting healthy physiologies. The effect of emphysematous destruction associated with COPD on the airflow patterns has not received as much attention. Oakes et. al. [57] and Berg [58] have conducted experiments of airflow in emphysematous alveolar models, identifying the influence of emphysematous destruction on particulate deposition and flow patterns formed in rat airways. However, the effect of emphysematous destruction on the close packed geometry on the acinus was not considered in the geometrical model. Recent work by Aghasafari et. al. [59] simulated the effects of emphysema on the partial closing of the terminal alveolar sacs through CFD, but the simulation neglected the influence of wall motion during the breath cycle. However, this model differed markedly from the close packed geometry that is being considered in this study. As such it only studied airflow in a cluster of alveoli at the end of a duct, without any branching thereby overlooking the variation in airflow caused in multi-generational geometries due to emphysema. Also, the primary focus of this investigation was the collapse and closure of the alveolar sacs due to emphysema and not the spetal destruction of the walls themselves. The most recent work to include a full numerical simulation of emphysema with multi-lobular geometry involves a study of aerosol deposition in healthy and emphysematous rat lungs [60]. In this study emphysema is simulated by the removal of inter-alveolar septa as well as changes in the lung motion and airflow rate, drawn from experi-

mental data. However, the conclusions drawn were based on the acinus as a whole and not at the level of individual ducts. Furthermore, the effects of emphysema on oxygen transport were not studied in detail and while some conclusions were drawn regarding particle depositions in emphysematous acini, they effects on particle-deposition patterns with progressively increasing levels of emphysema were not quantified.

CFD modelling is therefore potentially a powerful tool for studying complex phenomena such as emphysema, where multiple factors affect the airflow. CFD analysis not only allows the modeller to investigate the effects of individual symptoms of the disease, but also allows the study of the effects of the disease as it progresses in severity. This allows the investigation and prediction of airflow characteristics in a controlled manner that is difficult to replicate in experimental studies.

2.4 Summary

The human airway tree is a complex multi-scale structure which is primarily responsible for the transport of air from the atmosphere to the bloodstream. The smallest units of these airways are the pulmonary acini which are composed of alveolar structures arranged in a honeycomb like fashion around the terminal airways. The airways are surrounded by a complex network of elastic tissues which are responsible for providing mechanical support and the means for lung inflation.

Patients with emphysema have enlargement of their airspaces due to air-trapping. The progress of emphysema in the lung is heralded by the loss

of small airways in the distal ends of the pulmonary airway tree. The airways also lose their natural elastic recoil which contributes to the difficulty of the patient breathing out, resulting in the afore-mentioned air-trapping. Emphysema also causes significant changes in breathing patterns and quantifiable variables based on spirometry are currently used to diagnose COPD. However such techniques are not sensitive enough to detect emphysema in its earliest stages.

Computational Fluid Dynamics (CFD) is a powerful tool that has been widely utilized for studying human pulmonary airflow, diffusive transport of gases in the lungs and particle and aerosol transport and deposition in the airways. While there has been some initial research in employing CFD for the study of emphysematous alveoli, studies involving a complete model utilizing the mathematically derived 14-hedron geometry of the acinus and incorporating the effects of both parenchymal destruction and airway wall motion is lacking in the literature.

Chapter 3

Scope and Objectives

As explained in Chapter 2, the study of emphysema, especially in its earliest stages is hampered by the lack of suitable methods of diagnosis and the impossibility of performing *in vivo* study at the level of terminal bronchioles. CFD analysis, which has already been used for the study of healthy airways in the pulmonary acinus is uniquely suited to this task and therefore, has been chosen as the principal method of investigation here.

Therefore, the objectives of the study are to analyze the effects of emphysema on:

(a) The flow-field in the ducts and alveoli of the acinus.

(b) The transport of oxygen into the acinar airspaces during inspiration under the competing influences of diffusion and convection.

(c) The dynamics and deposition patterns of micron sized particles (d_p = 1 μm, 3 μm) in the acinus.

To achieve these objectives, a computational analysis of airflow is performed on a section representing the fourth and fifth generations of the pulmonary acinus which was geometrically modelled using the close-packed 14 hedron acinar geometry detailed in Section 2.1.2. The effects of emphysema

are incorporated into the overall computational model using a combination of three factors, (i) destruction of intra-alveolar septa, consistent with damage observed in emphysematous patients; (ii) reduction in airway wall motion, due to loss of parenchymal tissue matrix; (iii) reduction in airflow rate during the breath cycle which is a result of the loss of elastic nature of the airways. These conditions are meant to simulate the conditions in the airways in the earliest stages of emphysema.

Chapter 4

Methodology

4.1 Computational domain

To accurately capture the flow through the airways in a CFD study, physiologically realistic geometries, boundary conditions and wall deformations must be used. The closely packed alveolar structures in the acinar region are modeled using a geometry composed of fourteen sided polyhedrons (14-hedrons), following the work of Fung [7]. There are several examples of this geometry being used for CFD studies of alveolar airflow in literature [8, 10, 11, 41, 43]. The computational geometry for the present study is shown in Fig. 4.1. It consists of two generations of alveolar ducts that functionally correspond to the fourth and fifth generations of the pulmonary acinus after the start of the respiratory zone which approximately corresponds to the twenty-second and twenty-third generations from the trachea. Each duct models the alveolar spaces shaped as a 14-hedron, with 33 of these alveolar spaces in total. The collection of alveolar spaces that are ventilated by a single airway are herein referred to as a duct. As seen in Fig. 4.1, the domain consists of three ducts, one occurring proximal to the dichotomous branching and associated with the fourth generation of the pulmonary acinus (Duct 1), and two occurring distal to the dichotomous branching and

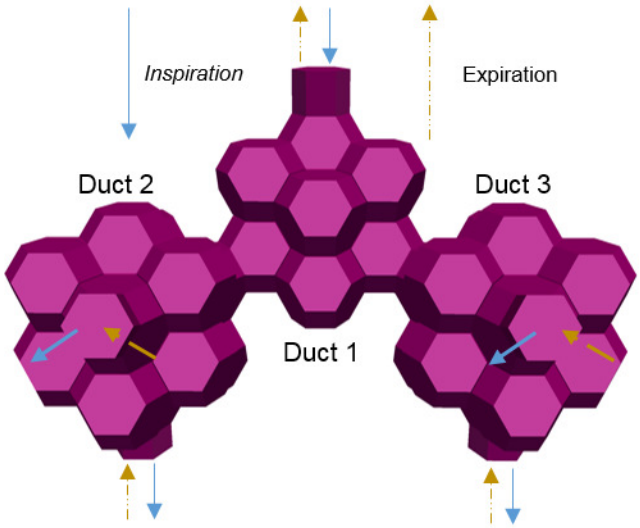

Figure 4.1: Computational domain of section of pulmonary acinus for present study. The blue and yellow arrows indicate the flow direction during inspiration and expiration, respectively.

associated with the fifth generation of the pulmonary acinus (Ducts 2 and 3).

The destruction of the septal walls between the alveolar spaces due to emphysematous progression is modelled in the present study by progressively removing septa in the three ducts of the computational geometry. As seen in Fig. 4.2, septal destruction progresses spherically from the centre of the duct towards the alveoli. The septa in each duct were degraded to the maximum extent possible without affecting the exterior of the geometry. This corresponds to the early stages of the disease in which large-scale destruction of the alveolar spaces has not yet occurred. Four cases were simulated to represent various stages in the progression of emphysema: Healthy, Stage I, Stage II, and Stage III. The healthy geometry has all of its septa

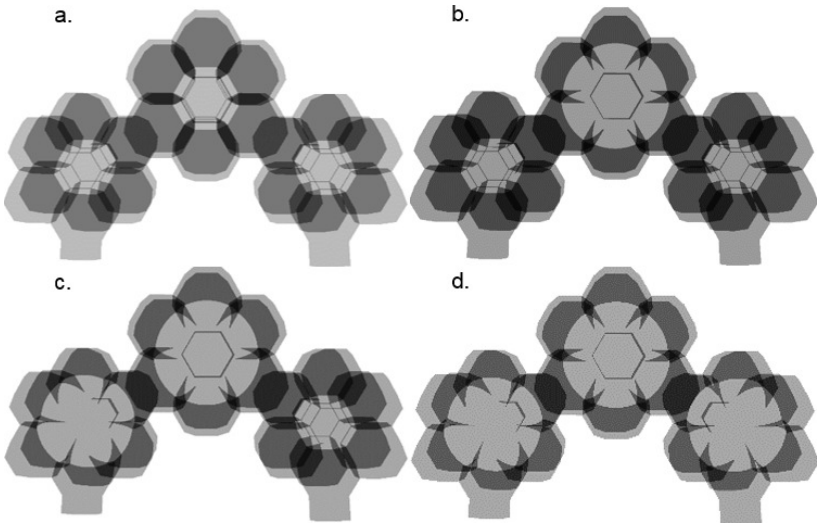

Figure 4.2: Progressive destruction of alveolar septa in the computational domain. (a) Healthy case (b) Case I (c) Case II (d) Case III.

intact, while Stages I, II and III have septal destruction in one, two, and three ducts, respectively.

4.2 Boundary conditions and wall motion

Boundary conditions for the computational domain consist of no-slip walls for all surfaces except the inflow and outflow boundaries. The boundaries defined at the entrances and exits to the ducts, labelled with arrows in Fig. 4.1, are defined as either inlet or outlet boundaries depending on the time of the simulation within the breath cycle. During the inspiratory phase, one inlet is defined at the entrance to Duct 1 and two outlets are defined for each of Ducts 2 and 3. During the expiratory phase, the situation reverses; two inlets are defined for each of Ducts 2 and 3, and one outlet is

defined for Duct 1.

To ensure accuracy of the present study, the boundary information defined at the inlet and outlet boundaries must reflect the actual physiology of the pulmonary acinus. Because *in vivo* measurements at this depth of the lung are impossible, the volume/flow rate relationships measured at the mouth must be used to infer flow rates in the pulmonary acinus. A typical volume/flow rate relationship at the mouth was already presented in Fig. 2.5 and can be approximated as follows. The flow rate during inspiration is

$$Q_{in} = Q_{in,\,max} \sin(\omega_p V) \quad \text{for} \quad 0 \leq V < V_{max} \tag{4.1}$$

and during expiration is

$$QQ_{exp} = \gamma V \quad \text{for} \quad V_{max,\,exp} \leq V < V_{max}, \tag{4.2}$$

$$Q_{exp} = -\beta V + \kappa \quad \text{for} \quad 0 \leq V < V_{max,\,exp} \tag{4.3}$$

where $Q_{in,\,max}$ is the maximum inspiratory flow rate, V_{max} is the maximum volume excursion of the lung/alveolus, ω_p is the breathing frequency (reciprocal of the breath period), $V_{max,\,exp}$ is the volume corresponding to maximum expiratory flow rate, and β, γ, and κ are constants. The effect of COPD on the volume/flow-rate relationship was also illustrated in Fig. 2.5. Although, the effects of COPD on the lung volume/air-flow rate relationship is not exclusively due to emphysema (Small Airways Disease (SAD) may also be a component) - due to the lack of available *in vivo* data from patients suffering exclusively from early stage emphysema, the boundary conditions

Table 4.1: Variation of parameters governing flow-rate and airflow motion due to emphysema

Case	$(L_m/2)$	β	κ	γ	Re_{insp}	Re_{exp}
Healthy	0.0265	-0.3816	0.0202	1.362	0.20	0.34
Case I	0.0236	-0.39672	0.0187	1.3032	0.18	0.30
Case II	0.0208	-0.41181	0.0171	1.2440	0.16	0.25
Case III	0.0179	-0.4269	0.0154	1.186	0.14	0.23

imposed on the simulation have been obtained from the interpolating the values between healthy and COPD observations in Fig. 2.5. This assumption might also justified due to the fact that SAD affects airways which are present higher in the airway tree than the acinus. Thus inflow conditions on the boundary of the diseased acinus should account for the combined effects of all the components of COPD. The effects of emphysema on the volume/airflow rate relationship may be summarised as follows. Emphysematous degradation leads to the loss of elastic recoil of the lung parenchyma. As a result, airways do not inflate as effectively and the maximum inspiratory flow rate and volume excursion at the end of inspiration is reduced. Due to the decreased elastic recoil, the expiratory flow rate also reduced. The reduction in flow rate can be modelled by altering the parameters β , κ, γ, V_{max} and $Q_{in,max}$ in Eqns. 4.1-4.3 according to Table 4.1. The extent to which the parameters are varied depends on the extent of emphysematous progression. As is clearly shown in Table 4.1, the progression of the disease is accompanied by a reduction in mesh motion and fall in the inlet Reynolds number. As mentioned before the values are obtained by interpolating between the healthy and COPD observations from Fig. 2.5

The airway wall-motion which drives the airflow in the airways during

breathing may be approximated as self-similar [39], meaning that the temporal variation of any length scale $L(t)$ with respect to a reference length L_0 is given by

$$L(t) = L_0 \left[1 + \frac{L_m}{2} + \frac{L_m}{2} \sin\left(\omega_p\, t - \frac{\pi}{2}\right)\right]. \tag{4.4}$$

By defining a parameter λ equal to the bracketed expression on the right hand side of Eqn. 4.4, the above expression can be simplified as

$$L(t) = L_0 \lambda.$$

The length scale L_m in Eqn. 4.4 is defined as

$$L_m = (C+1)^{\frac{1}{3}} - 1 \tag{4.5}$$

where C is defined as the ratio of tidal lung volume to the functional residual capacity (FRC),

$$C = \frac{V_t}{FRC}. \tag{4.6}$$

The variation of the alveolar volume with time is therefore given by

$$V(t) = V_0 \lambda^3. \tag{4.7}$$

The variation in the alveolar volume is implemented in the simulations through a user-defined function (UDF), reproduced in Appendix A, which expands and contracts the cells within the computational mesh in a manner given by Eqn. 4.7. Figure 4.3(a) plots the resulting relative displacement of

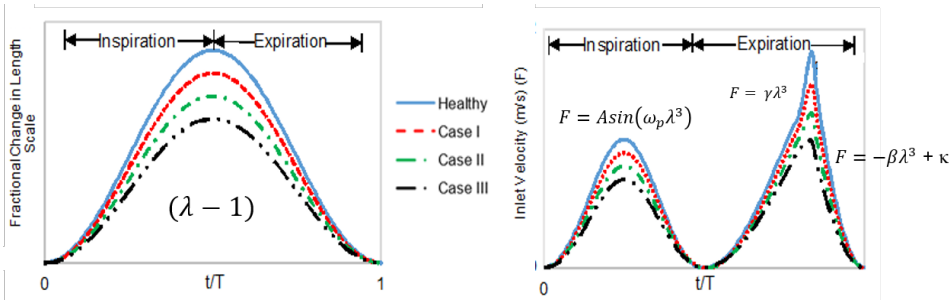

Figure 4.3: (a) Displacement of the airway wall from rest during inspiriation and expiration for the healthy and diseased cases. (b) Temporal variation of flow rate into the pulmonary acinus during inspiration and expiration for the healthy and diseased cases.

the airway wall for the four simulated cases during inspiration and expiration. It should be noted that the values on the y-axis represent the relative change from the resting position of the lung. The values are obtained by substituting the constants from Table 4.1 into Eqn. 4.7. The motion of the alveolar walls affects the flow rates into and out of the computational domain derived in Eqns. 4.1-4.3. In order to capture this effect, Eqn. 4.7 needs to be substituted into Eqn. 4.1-4.3. The resulting inspiratory flow rate is

$$Q_{in} = Q_{in,\,max} \sin\left(\omega_p \lambda^3\right) \quad \text{for} \quad 0 \leq t < t_{insp} \tag{4.8}$$

and the expiratory flow rate is

$$Q_{exp} = \gamma \lambda^3 \quad \text{for} \quad t_{insp} \leq t < t_{exp,\,max} \tag{4.9}$$

$$Q_{exp} = -\beta \lambda^3 + \kappa \quad \text{for} \quad t_{exp,\,max} \leq t < t_{exp}. \tag{4.10}$$

These equations were imposed at the inlet boundaries of the computational

domain as temporally-varying inflow velocity conditions. At the outlet boundary, a zero gauge static pressure condition is defined. These flow rate relationships are shown in Fig. 4.3(b) for the four simulated cases. The values of the velocity at the inlet have been reported as scalars and it should be noted that during expiration the air flows out of the domain. It is also notable that the largest deviation from the healthy case occurs for Case 3, as it has the largest degradation of the septa. The breath-cycle time period τ for all simulations was chosen to be 3 seconds in accordance with similar studies available in literature [11, 39]. This corresponded to a breathing-cycle period of $\omega_p = 2.094$. This value of breathing-period corresponds to fairly quick breathing which corresponds to light exercise.

In healthy human lungs, the alveolar walls are richly supplied by blood capillaries, and function as sites of gas exchange between the inspired air and the bloodstream. A concentration gradient exists at the alveolar-capillary interface which allows the exchange of oxygen and carbon-dioxide by diffusion. Computationally, Sapoval et. al. demonstrated that this may be thought of as a gradient dependent on oxygen and carbon dioxide concentration close to the alveolar-capillary boundary [61]. This gradient when imposed on the walls of computational domain,enhances the diffusive transport of oxygen towards the walls during inspiration and carbon dioxide away from the walls during expiration, which mimics the physiological process of gas-exchange in actual lungs. Such an approach was used by Hofemeier et. al. [62] in their latest work simulating airflow changes in acinar structures from infancy to adulthood where a constant gradient was assumed for the wall-flux of oxygen. However, such an approach is imperfect, as this

gradient is actually highly time-dependent and changes rapidly during the breath-cycle [5]. Furthermore, the flow throughout the entirety of the acinus is not diffusive but significant convective transport may occur in the more proximal generations of the alveolus during inspiration. In fact, available literature [63] suggests that the transition point during sedentary breathing for convective and diffusive transport is the fourth and fifth generation of the acinus. For heavier breathing, which is simulated in the present study, this transition point may move deeper into the acinus. In the present study, the computational domain was chosen to be the fourth and fifth generations of the acinus. This fact coupled with a lower breathing time period means that during a majority of the inspiratory cycle, the transport of the oxygen throughout the domain is primarily carried out by convection rather than diffusion. In addition to this the probe points for recording changes in oxygen concentration are located near the alveolar entrances, well away from the walls. These two factors justify the decision to not model the diffusive transport of oxygen and carbon dioxide through the walls. Additionally, the precise effects of emphysematous destruction on the alveolar-capillary diffusion are not known and thus could not have been correctly modeled as a factor in simulating progressive emphysema.

4.3 Spatial mesh

The geometry was meshed using ANSYS ® Meshing (Release 15.0) commercial software and the resulting mesh is shown in Fig. 4.4. An unstructured meshing algorithm using tetrahedral elements was adopted. Care was

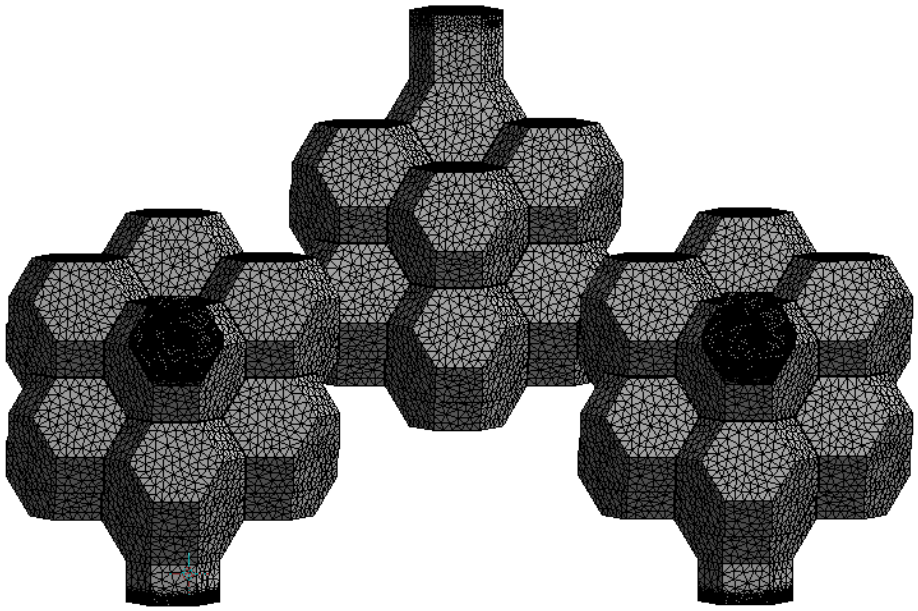

Figure 4.4: Computational mesh composed of tetrahedral elements. Note refined areas at inlet and outlet

Table 4.2: Mesh independence study, with the observed variable being the static pressure drop across Duct I

Mesh	Mesh elements	Static pressure (Pa)	% change
1	500,000	0.00325	—
2	600,000	0.00332	2.15
3	700,000	0.00335	0.09

taken to refine the mesh at the inlet(s) and outlet(s) as shown in Fig. 4.4. A mesh-independence study was carried out with sucessively refined meshes as shown in Table 4.2, with the static pressure in Duct 1 being the monitored parameter to establish grid independence The finest mesh was composed of 700,000 elements. It was observed that the monitored quantity changed by only 0.09 % thereby showing that the mesh with 700,000 elements achieves suitable accuracy while ensuring reasonable solution times.

4.4 Solution approach

4.4.1 Continuity and momentum equations

The determination of a flow field requires the solution of the continuity (Eqn. 4.11) and momentum transport equations (Eqn. 4.12) along with the solutions of the transport equations of any other quantity of interest. These equations are

$$\frac{\partial \rho}{\partial t} + \nabla.(\rho \boldsymbol{u}) = 0 \tag{4.11}$$

$$\frac{\partial \rho \boldsymbol{u}}{\partial t} + \nabla(\rho \boldsymbol{u}\boldsymbol{u}) = -\nabla p + \nabla.\boldsymbol{\tau} + \rho \boldsymbol{g} \tag{4.12}$$

where $\boldsymbol{\tau}$ represents the stress tensor. In the present study the commercial solver ANSYS ® Fluent (Release 15.0) was used to solve the above equations using the finite volume method, which is described in detail in the subsequent sections.

4.4.2 Finite volume method

Integral formulation

In the finite volume method the integral forms of the continuity and momentum transport equations are applied over each control volume or element that makes up the mesh of the computational domain.

$$\oint_V \frac{\partial(\rho \boldsymbol{u})}{\partial t}.dV + \oint_A (\rho \boldsymbol{u}).d\boldsymbol{A} = 0 \tag{4.13}$$

$$\oint_V \frac{\partial(\rho \boldsymbol{u})}{\partial t}.dV + \oint_A (\rho \boldsymbol{u}\boldsymbol{u}).d\boldsymbol{A} = -\oint_A p.\boldsymbol{I}.d\boldsymbol{A} + \oint_A \boldsymbol{\tau}.d\boldsymbol{A} + \oint_V \rho \boldsymbol{g}.dV, \quad (4.14)$$

where the subscripts V and A indicate integrals over the volume and surface of the domain in question and I being the identity matrix.

Spatial discretization

The integral forms of the governing equations may then be discretized in order to transform them into a system of linear equations. For the momentum and continuity equations this leads to a total of 4 equations, one for each component of the velocity (Eqns. 4.15a, 4.15b, 4.15c) and the continuity equation (Eqn. 4.16):

$$a_P u = \sum_{nb} a_{nb} u_{nb} + \sum p_f \boldsymbol{A}.\hat{i} + S_u \quad (4.15a)$$

$$a_P v = \sum_{nb} a_{nb} v_{nb} + \sum p_f \boldsymbol{A}.\hat{j} + S_v \quad (4.15b)$$

$$a_P w = \sum_{nb} a_{nb} w_{nb} + \sum p_f \boldsymbol{A}.\hat{k} + S_w \quad (4.15c)$$

$$\sum_{N_{faces}} J_f A_f = 0 \quad (4.16)$$

The coeffcients a_p and a_{nb} represent known values at the cell centre in question and that of its immediate neigbours.

The nature of the discretization dictates that the pressure and mass flux at the cell faces be known in order to solve the equations. ANSYS

Fluent uses a co-located scheme where both the pressure and cell velocities are both stored at the cell centres. However such a scheme is prone to unphysical "checkerboarding" of pressure and velocities. This is overcome by the method outlined by Rhie and Chow [64]. Therefore, in order to calculate the face flux $J_f = \rho u_{nf}$ where u_{nf} is the normal velocity through the face f, instead of using linear interpolation a momentum weighted average is used:

$$J_f = \rho_f \frac{a_{p,c_0} u_{n,c_0} + a_{p,c_1} u_{n,c_1}}{a_{p,c_0} + a_{p,c_1}} + d_f((p_{c0} + \nabla p_{c0}.\boldsymbol{r_0}) - (p_{c1} + \nabla p_{c1}.\boldsymbol{r_1})) \quad (4.17)$$

where $u_{n,c_0}, u_{n,c_1}, p_{c0}, p_{c1}$ are the pressures and normal velocities at the cell centres on either side of the face and d_f is a function of the average of the two momentum coefficients a_{p,c_0} and a_{p,c_1} (from Eqn. 4.15) on either side of the face. The pressure values at the cell faces are interpolated in the following manner:

$$p_f = \frac{\frac{p_{c0}}{a_{p.c0}} + \frac{p_{c1}}{a_{p.c1}}}{\frac{1}{a_{p.c0}} + \frac{1}{a_{p.c1}}} \quad (4.18)$$

Pressure velocity coupling

While the discretization of the continuity and momentum equations provide four equations (Eqns. 4.15- 4.16), the continuity equation does not have any pressure terms and thus the pressure field needs to be coupled to the velocity field in order to solve for the pressure field. In the present case, the semi-implicit method for pressure-linked equations (SIMPLE) scheme originally described by Patankar [65] is used for this. The SIMPLE algorithm uses a relationship between velocity and pressure corrections to enforce mass conservation and to obtain the pressure field. The momentum equation is

first solved with a guessed pressure field p^*, which results in a face-flux J_f^* that does not satisfy the continuity equation. The corrected flux is then obtained by adding a correction factor $J_f^{'}$ defined as

$$J_f = J_f^* + J_f^{'} \tag{4.19}$$

The SIMPLE algorithm then postulates that the correction factor $J_f^{'}$ be expressed as

$$J_f^{'} = d_f(p_{c0}^{'} - p_{c1}^{'}) \tag{4.20}$$

where $p^{'}$ is the cell pressure correction. When Eqns. 4.20 and 4.19 are substituted into 4.16 we get a discretized equation for the pressure correction terms as follows

$$a_p p^{'} = \sum_{nb} a_{nb} p_{nb}^{'} + \sum_{N_{faces}} J_f^* A_f \tag{4.21}$$

All the terms in Eqn 4.21 except for $p^{'}$ are known. Once the lone unknown is determined the corrected pressure is determined as

$$p = p^* + \alpha_p p^{'} \tag{4.22}$$

where α_p is the under-relaxation factor. The corrected face flux which satisfies the continuity equation is then obtained as

$$J_f = J_f^* + d_f(p_{c0}^{'} - p_{c1}^{'}) \tag{4.23}$$

Temporal discretization

Temporal discretization involves the integration of every term in the differential equations over a time step Δt. For any generic variable ϕ and a first order time evolution given by

$$\frac{\partial \phi}{\partial t} = F(\phi) \tag{4.24}$$

The equation can be discretized in time to second order (as is used in the current model) as follows

$$\frac{3\phi^{n+1} - 4\phi^{n} + \phi^{n-1}}{2\Delta t} = F(\phi) \tag{4.25}$$

where the superscripts $n-1, n, n+1$ denote the previous,current and future time levels respectively. The simulation was integrated in time with a time step size of $\Delta t = 10^{-4}$ seconds, which satisfies the CFL condition for all times within the breath period. At each time step, the algebraic system of equations are solved iteratively until the root-mean-square residuals for continuity, momentum conservation, and species mass fraction converge to less than 10^{-6}, which is achieved in approximately 20 coefficient loop iterations per timestep on average. The temporal algorithm for the entire solution is best described by the means of the flowchart shown in Fig. 4.5

4.4.3 Scalar transport

A scalar transport equation was also solved in order to track the transport of respiratory gases into and out of the computational domain. The

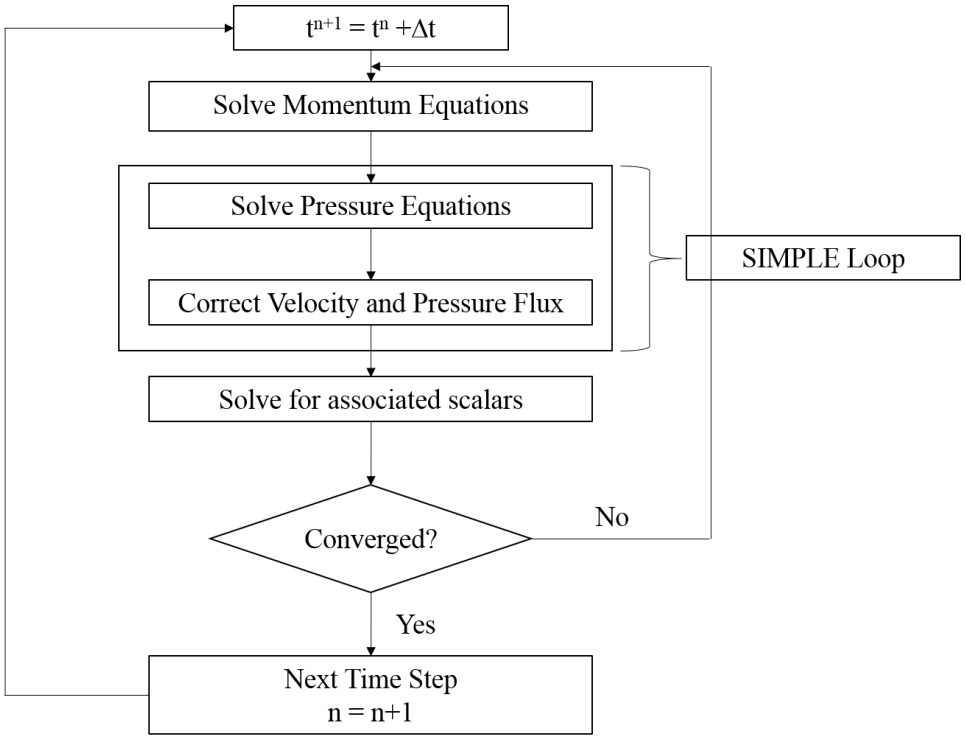

Figure 4.5: Solution Algorithm

passive transport of gas concentration is given by

$$\frac{\partial(\phi_i)}{\partial t} + \nabla(\vec{v}.\phi_i) = -\frac{1}{\rho}\nabla \cdot \vec{J_i} \tag{4.26}$$

where ϕ_i is the concentration for each species in the domain and J_i is the corresponding flux of the species given by Fick's law as shown in Equation 4.27

$$\vec{J_i} = -\rho D_i \nabla Y_i \tag{4.27}$$

The diffusive coefficient of oxygen within air for this simulation (D_i) has a value of 0.213 cm^2/s.

In order to determine the values of the scalar ϕ at the cell faces, a second order upwinding (SOU) technique is used:

$$\phi_{f,SOU} = \phi + \nabla\phi.\boldsymbol{r} \tag{4.28}$$

where ϕ and $\nabla\phi$ are the values of the scalar and its gradient at the cell upstream of it with $\boldsymbol{r}$ is the displacement vector from the upstream cell centroid to the face centroid.

The incoming air was assumed to be composed solely of nitrogen, oxygen, carbon dioxide and water vapor with volumetric fractions of 0.78,0.21,0.0004 and 0.0096 respectively. The exhaled air had reduced oxygen and increased carbon dioxide and water vapor with volumetric fractions of 0.15,0.04 and 0.03 respectively with the nitrogen fraction remaining unchanged. The initial conditions in the computational domain were assumed to be identical to that of the expelled air.

4.4.4 Particle transport

The particle dynamics in the computational domain are governed by a balance of convective and gravitational forces given by Eqn. 2.5 in Section 2.1. These equations were integrated over time in order to determine the trajectories of inhaled particles. Eqn. 2.5 may be restated in a simplified form (for one velocity component) as follows:

$$\frac{du_p}{dt} = \frac{(u_p - u_f)}{\tau} + a \tag{4.29}$$

where τ represents the drag force coefficients and a represents all other external forces , which in this thesis consists of the gravitational force only but in general may include other forces related to Brownian motion if the particle is very small. The position of a particle is given by

$$\frac{dx_p}{dt} = u_p \tag{4.30}$$

Equations 4.30 and 4.29 are therefore coupled and need to be simultaneously integrated in order to determine the particle trajectories. An explicit Euler temporal discretization is applied to Eqn 4.29 to yield

$$u_p^{n+1} = \frac{u_p^n + \Delta t(a + u_f^n/\tau)}{1 + (\Delta t/\tau)} \tag{4.31}$$

while a trapezoidal discretization is applied to solve for x_p

$$x_p^{n+1} = x_p^n + \frac{\Delta t(u_p^n + u_p^{n+1})}{2} \tag{4.32}$$

During the simulation, particles were introduced into the domain from the inlet from $\tau = 0$ to $\tau = 0.5$, with τ defined as the instantaneous time normalised over one breath-period i.e. $\tau = t/T$.

Since the orientation of the gravity vector has been shown to have considerable influence on the particle trajectories and hence deposition, simulations were conducted for two cases where the gravity vector was oriented normal and tangential to the entrance of the solution domain respectively.

4.4.5 Initial conditions

The solutions were initialized with a zero velocity field and at atmospheric pressure mimicking conditions immediately preceding the start of inspiration. The initial mass fraction of oxygen inside the alveolar ducts is 0.15, which corresponds to the oxygen-poor condition that exists at the completion of expiration. Each breath period was 3 seconds long corresponding to a breathing frequency of 20 breaths per minute.

4.4.6 Solution hardware

This solution approach was computed in parallel using a message-passing interface (MPI) using 6 virtual cores of an Intel Xeon CPU with a clock-speed of 2.50 GHz such that the average simulation time for one complete breath period was approximately 4.5 hours.

Chapter 5

Results and Discussion

5.1 Overview

This chapter details the results obtained from the simulations described in Chapter 4. The results and the discussions that accompany them have been presented in a manner that meets the objectives detailed in Chapter 3. They have been divided into two sections each of which discusses the nature of the results obtained and then presents the effects of advancing emphysema on those results. The first section discusses the oxygen transport and general nature of the flow-field into the acinus, while the second details the nature of particle deposition dynamics in the respiratory zone and the effects of emphysema on the observed deposition parameters.

5.2 Flow field and oxygen transport

5.2.1 Oxygen transport

The mass fraction of oxygen inside the computational domain increases during inspiration due to convective and diffusive transport of oxygen-rich air from the inlet into the alveoli. To monitor the average oxygen concentration within the three ducts of the computational domain, twelve sampling

points are arranged with four points within each duct. Each sampling point is equidistant from the inlet of the domain and arranged in a radially symmetrical fashion along the axis of the flow. As a result, the average of the readings from the four sample points within a duct for each time step represents a measure of oxygen transported to the alveolar spaces of that duct up to that time step. From these sampling points, the percentage increase of oxygen mass fraction averaged over the four sampling points within each duct, denoted $\overline{C}$, can be defined as

$$\overline{C} = \frac{1}{4}\sum_{n=1}^{4}\left(\frac{C_{t,\,n} - C_o}{C_o}\right) \times 100\% \tag{5.1}$$

where $C_{t,\,n}$ is the mass-fraction of oxygen at time t at sampling point n and C_o is the initial mass-fraction of oxygen in the domain at the start of inspiration. The temporal variation of $\overline{C}$ during inspiration for each duct is plotted in Fig. 5.1. The trends obtained in Fig. 5.1 clearly show that oxygen transport through all three ducts is severely reduced with the progress of emphysematous destruction and the associated reduction in airway wall motion and flow rate. This provides a qualitative explanation of ventilation-perfusion mismatch (conditions where there is an imbalance between the oxygen transported into the lung and blood circulated through it) difficulties that are commonly reported in patients with emphysema [66]. Figure 5.1 also shows that there is a phse-shift in the time-signal of oxygen mass fraction between the proximal and distal generations of the computational domain. The proximal generation (Duct 1) reaches a maximum $\overline{C}$ value at $t/T = 0.3$ while the distal generation (Ducts 2 and 3) have an

increasing value of $\overline{C}$ until the end of inspiration. This is explained by the fact that Ducts 2 and 3 are distal to Duct 1 and thus receive oxygen later in the inspiratory cycle.

In order to determine the individual effects of septal destruction and the decrease in airway wall motion and accompanying loss in inlet air-flow rate, parametric studies are performed in which these two effects are turned on or off independently. Figure 5.2 plots the temporal variation of $\overline{C}$ for simulations in which only septal degradation is present, and the airway wall motion and inlet flow rates equal those in the healthy case. For, each duct, very little difference in the transport of oxygen into the alveoli is noted between the healthy and diseased cases despite the significant differences in the degree of septal degradation between the four cases. Fig. 5.3 plots the temporal variation of $\overline{C}$ for simulations in which no septal degradation is present and only the emphysematous degradation of airway wall motion and flow rates are included. The trends noted in Fig. 5.3 mirror those in Fig. 5.1 for which all features of the disease are included. This suggests that the factors primarily responsible for the decreasing oxygen transport into emphysematous acini are the reduction in airway wall motion and flow rate; as septal destruction has a negligible impact on the reduced oxygen transport.

5.2.2 Hydraulic losses

In order to characterize the effect of emphysema on the flow-related pressure drop, termed the hydraulic loss, the average drop in static pressure through each alveolar duct is computed. While the total pressure is a more

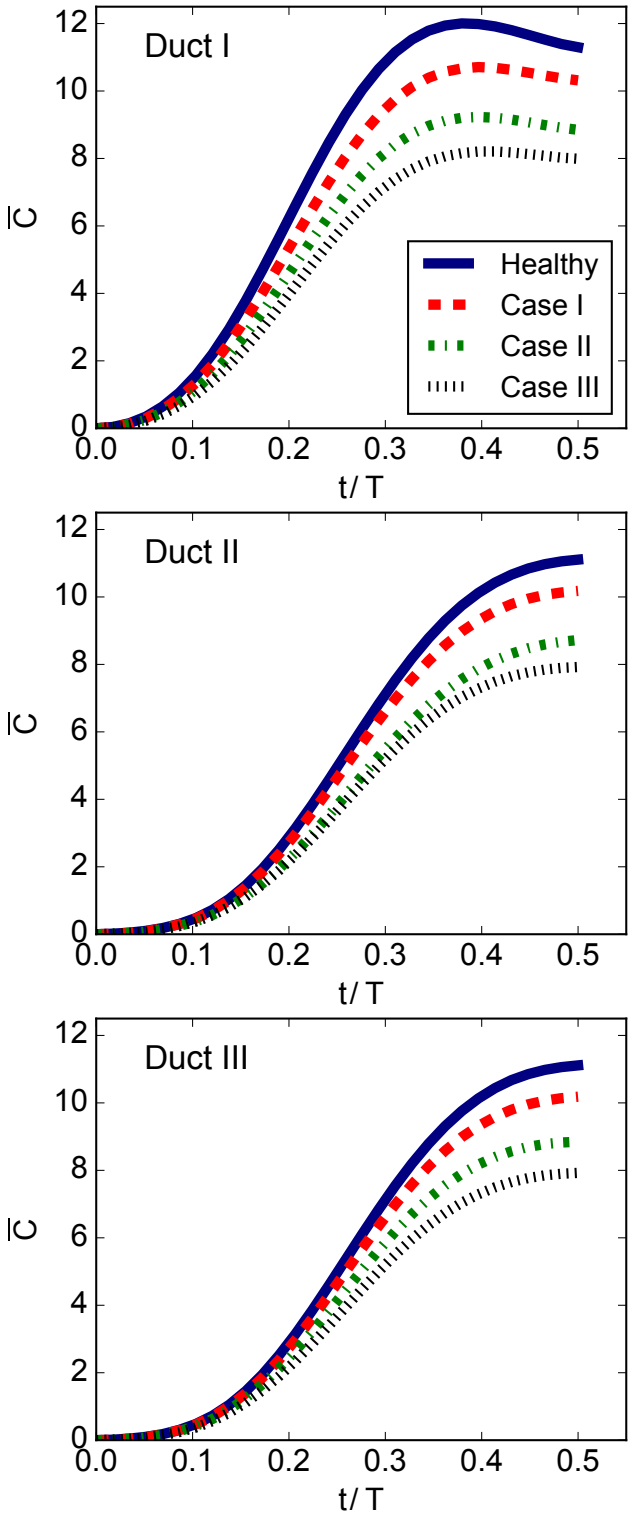

Figure 5.1: Temporal variation of the percentage increase in oxygen concentration within a duct ($\overline{C}$) for cases with both septal destruction and emphysematous wall motion/inlet flow rates.

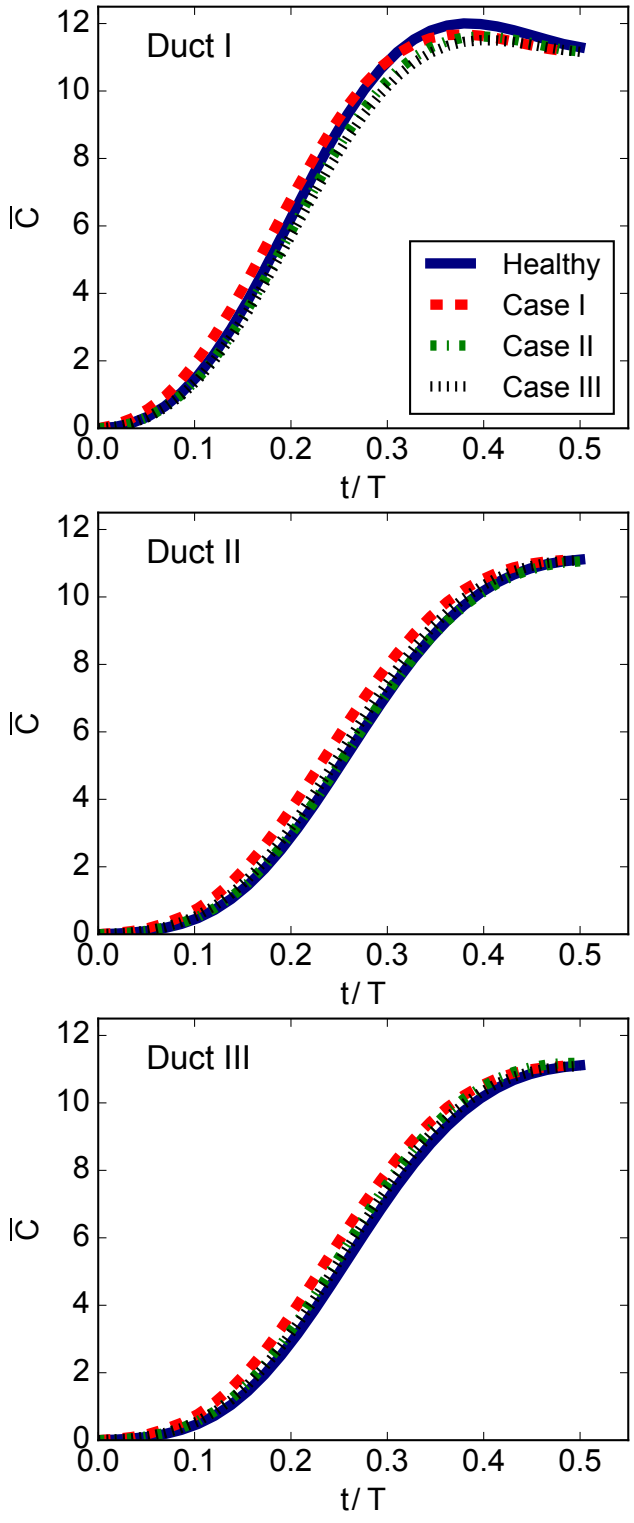

Figure 5.2: Temporal variation of the percentage increase in oxygen concentration within a duct ($\overline{C}$) for cases with only emphysematous septal destruction.

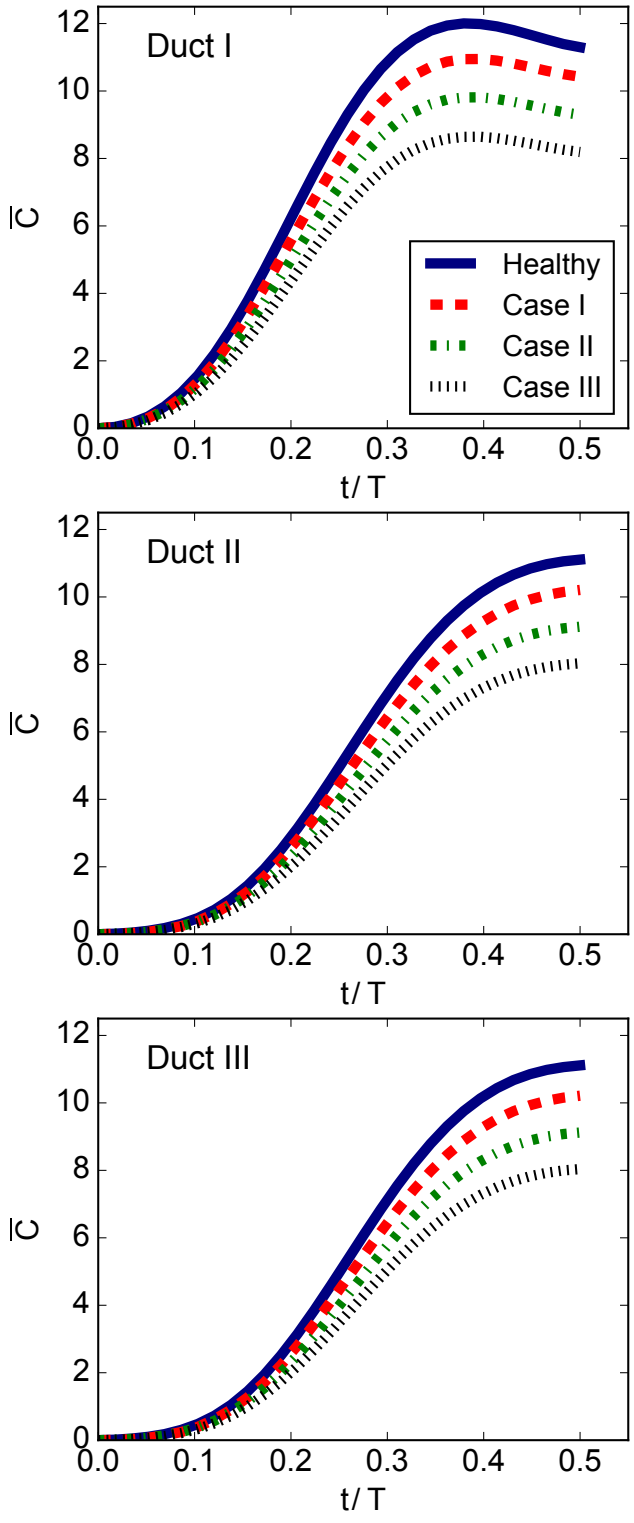

Figure 5.3: Temporal variation of the percentage increase in oxygen concentration within a duct ($\overline{C}$) for cases with only emphysematous wall motion/inlet flow rates.

appropriate metric for assessing hydraulic loss, the extremely low velocities within the pulmonary acini generate dynamic pressures that are smaller than 10^{-3} times the static pressure, and thus the static pressure is a very close approximation of the total pressure. The average pressure drop for each duct is computed as the difference in static pressure between the one inlet and the average of the two outlets during inspiration, and the average of the two inlets and one outlet during expiration. The pressure values are obtained from probes located at the spatial center of the inlets and outlets of each duct, which were shown in Fig. 4.1.

The temporal variation in the pressure drop across the three ducts during inspiration is shown in Figs. 5.4-5.6. As in Figs. 5.1-5.3, Fig. 5.4 plots the results for simulations in which both septal degradation and emphysematous wall motion and inlet flow rates are present, and Figs. 5.5 and 5.6 plot the results for simulations with only septal destruction and only emphysematous degradation in wall motion and flow rates, respectively. Figure 5.4 shows that the pressure drop through all ducts varies almost sinusoidally during inspiration with a maximum at the point of maximum inspiratory flow rate and approaching zero at the start and end of inspiration. This is consistent with losses varying directly with the flow rate, i.e. velocity-squared losses. Comparing Duct 1 and Ducts 2 and 3 in Fig. 5.4, the lower pressure drop through Ducts 2 and 3 is because the flow rate reduces past the dichotomous branching. It is notable that the pressure drops through Ducts 2 and 3 are equal for the Healthy, Case I, and Case III cases, but for Case II, a larger pressure drop occurs across Duct 2 than Duct 3. Because Case II has septal destruction in Duct 2 but not in Duct 3, the flow resistance through

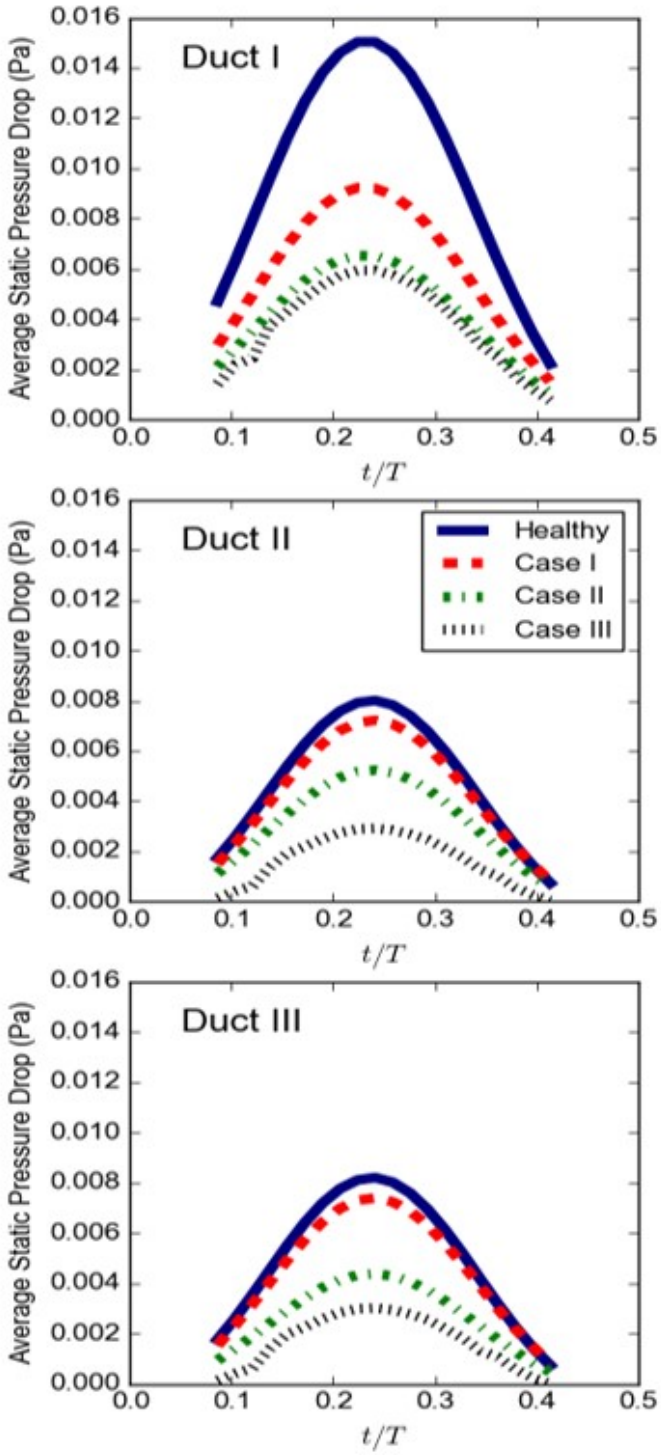

Figure 5.4: Temporal variation in the static pressure drop across the alveolar ducts for cases with both septal destruction and emphysematous wall motion/inlet flow rates.

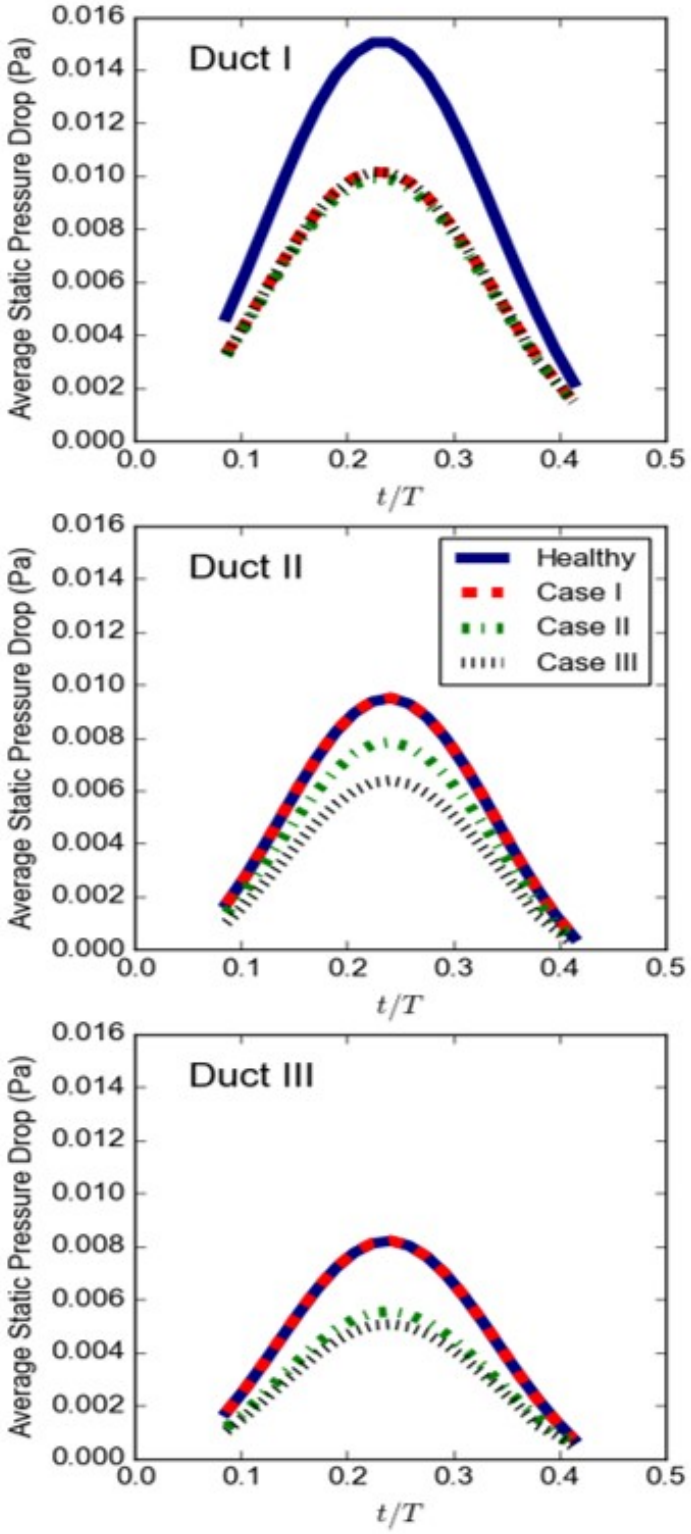

Figure 5.5: Temporal variation in the static pressure drop across the alveolar ducts for cases with only emphysematous septal destruction.

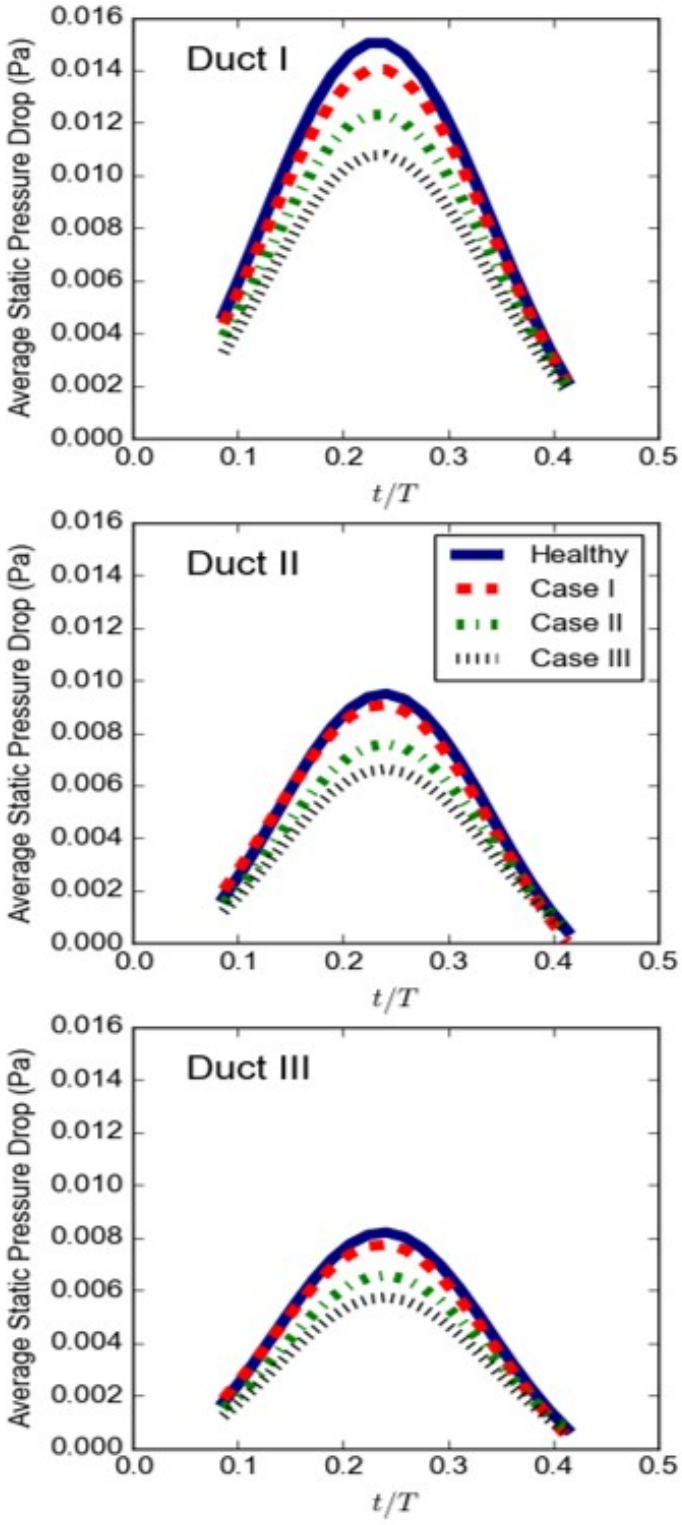

Figure 5.6: Temporal variation in the static pressure drop across the alveolar ducts for cases with only emphysematous wall motion/inlet flow rates.

Duct 2 is lower than through Duct 3, resulting in the flow preferentially tending towards Duct 2. The increased velocity through Duct 2 results in the observed increased static pressure drop relative to Duct 3. The velocities through the ducts are discussed in more detail in section 5.1.4.

Further insight into the mechanism behind hydraulic losses through the pulmonary acini is found by considering the independent effects of septal destruction and emphysematous wall motion and flow rates. In Fig. 5.5, only septal destruction is considered; the wall motion and flow rates equal those in the healthy case. Comparing the healthy and diseased cases in Duct 1 shows that the removal of septa reduces the static pressure drop through the duct. This result is somewhat counter intuitive, as emphysema is associated with increased difficulty in breathing. It indicates that destruction of the intra-alveolar septa makes the duct less resistive to the flow and thus produces lower hydraulic loss through the duct. In Ducts 2 and 3, there is no septal destruction for Case I, hence it exactly follows the healthy case, while the difference between Duct 2 and 3 in Case II is caused by the asymmetry in the flow resistance and velocity between the ducts, noted earlier. In contrast, when only the emphysematous wall motion and inlet flow rates are considered (Fig. 5.6), the pressure drop through the alveolar ducts is much higher than in the cases where only septal destruction occurs. Within each duct, a steady reduction in the pressure drop is noted between the healthy and diseased cases, consistent with the reduction in inlet flow rates for each case. This suggests that hydraulic losses through the emphysematous acini are influenced primarily by the loss of intra-alveolar septa. The loss in septa reduces the hydraulic losses through the alveolar ducts, and the reduced

flow rates and wall motion due to emphysema has a secondary importance on the hydraulic loss. Similar results were also obtained for the expiratory breathing phase.

5.2.3 Flow field visualization

The complexity of the spatial geometry and the temporally-varying nature of the wall motion and inlet flow rates makes the complete characterization of the flow field through the acinus very challenging. Therefore, attention is given primarily to the patterns that develop in the ducts and alveolar spaces at peak inspiration and expiration.

Figures 5.7 and 5.8 plots streamlines coloured by the velocity magnitude (U) in planes that bisect the computational domain at peak inspiration and expiration, respectively.

It may be noted that in Case II (Figs. 5.7(c) and 5.8(c)), the velocities in Duct 2 with emphysematous destruction are much higher than Duct 3 with healthy septa. This is because the removal of the septa decreases overall resistance to the flow, which in turn causes the higher velocities in Duct 2. It should not be concluded that emphysematous destruction leads to an increase in flow rate through the acinus. As previously described, the inspiratory and expiratory flow-rates are coupled to the negative and positive pleural pressures generated in the acini during breathing by the parenchymal mesh that surrounds the acinus. The degeneration of the parenchyma in emphysema results in reduced pleural pressures and correspondingly lower flow rates. As a result, emphysema reduces flow resistance through the airway via septal destruction while also simultaneously reducing the overall

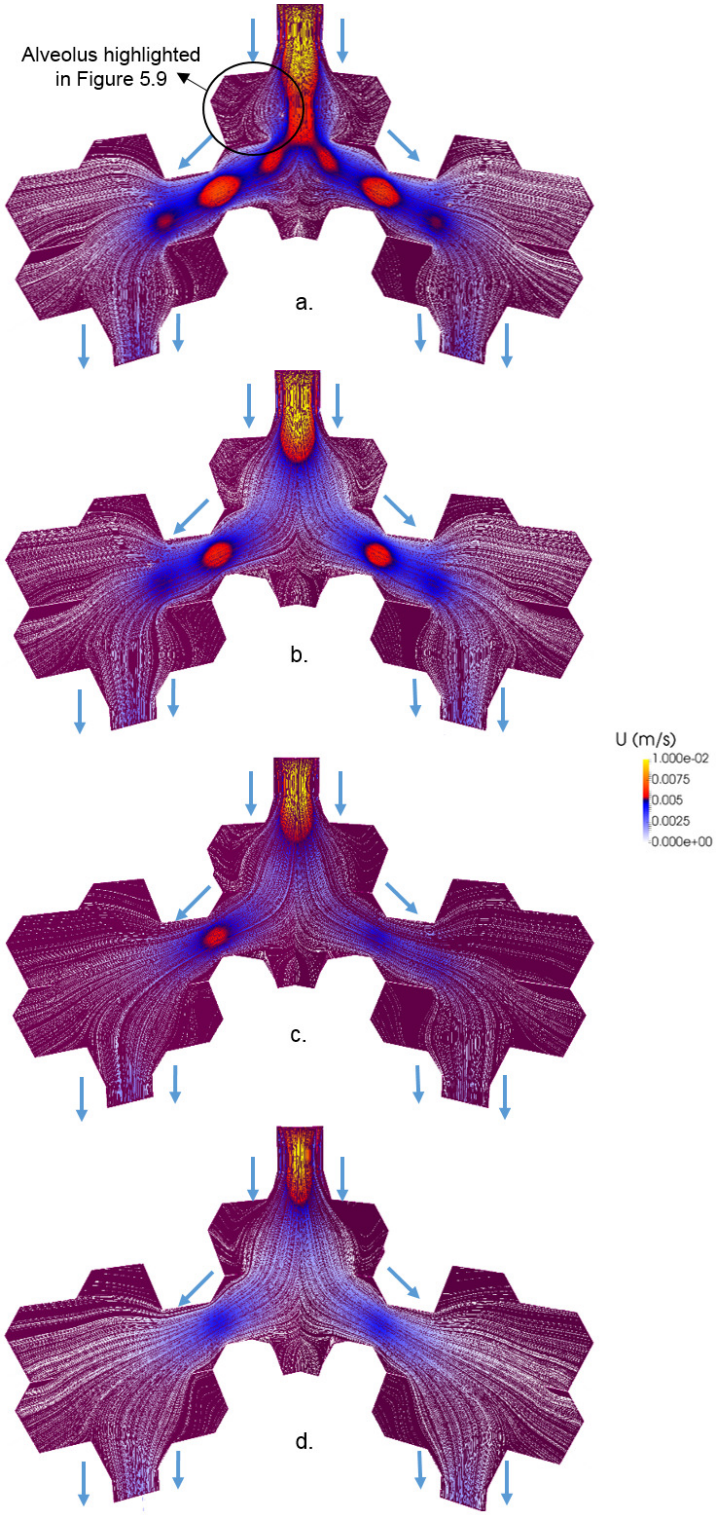

Figure 5.7: Velocity contours at peak inspiration (a) Healthy case (b) Case I (c) Case II (d) Case III. Arrows indicate general flow direction in the acinus.

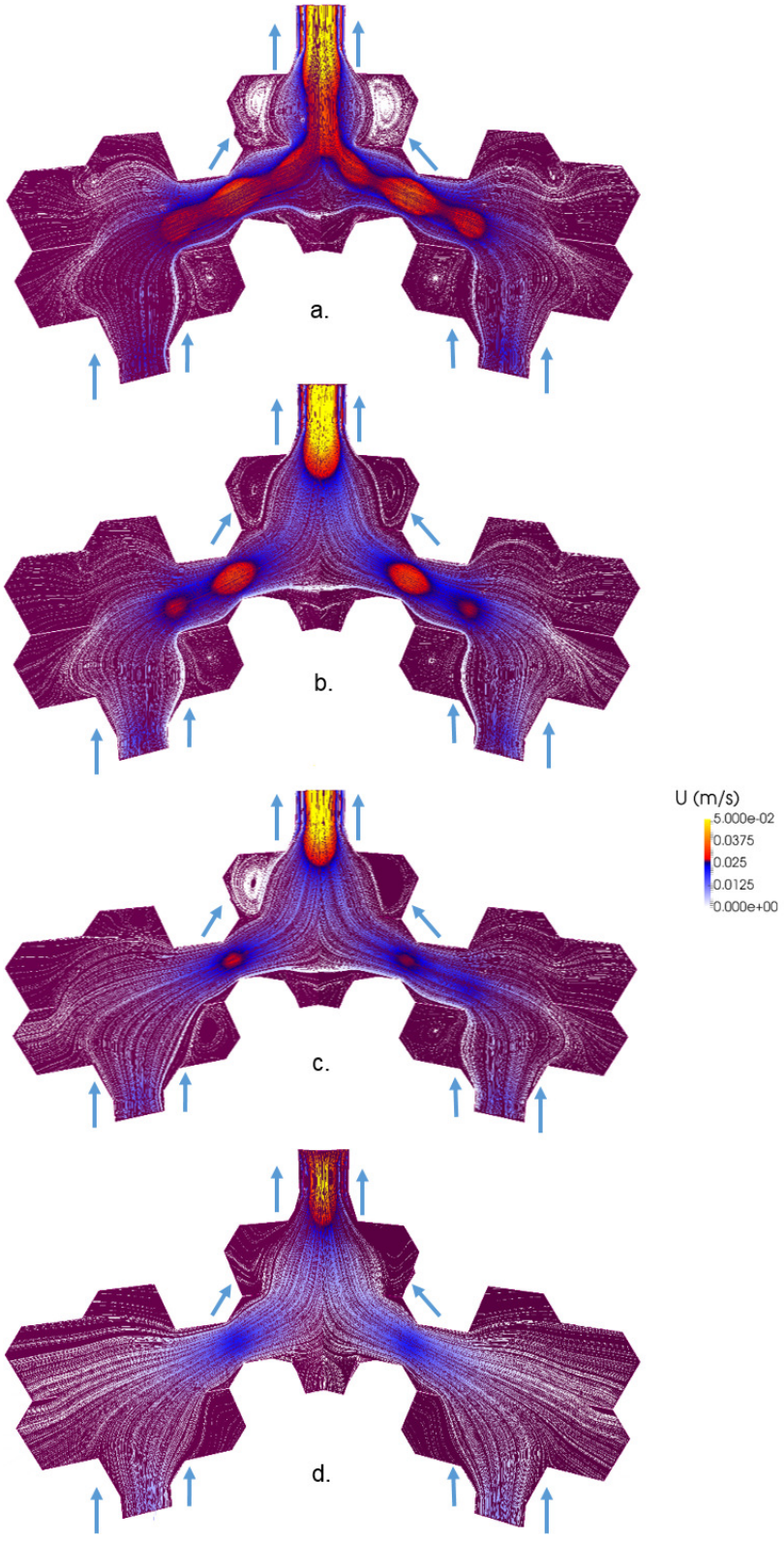

Figure 5.8: Velocity contours at peak expiration (a) Healthy case (b) Case I (c) Case II (d) Case III. Arrows indicate general flow direction in the acinus.

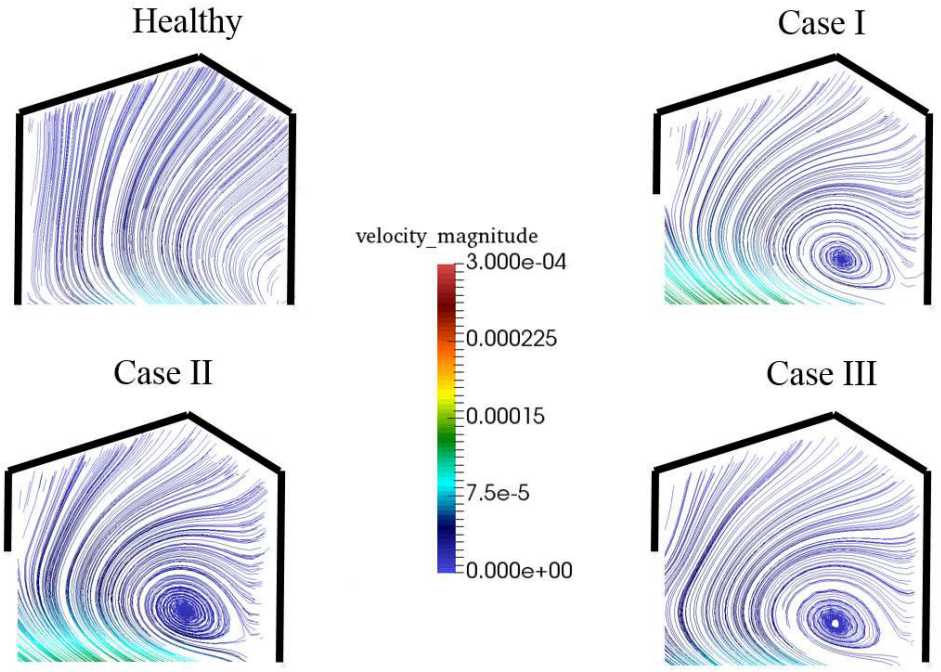

Figure 5.9: Streamlines in an individual alveolus from Duct 1 near the end of inspiration for the healthy and diseased cases. Streamlines are coloured according to velocity magnitude.

flow rates via degeneration of the elastic parenchymal tissue. From Figs. 5.7 and 5.8 it is apparent that velocities within the cavities are on average one or two orders lower in magnitude than the main flow in the duct, which also accords well with previously published results [8, 39]. As such, due to their low inertia, the flow patterns in the alveolus are highly susceptible to change based on the conditions in the duct. This is illustrated in Fig. 5.9 for the alveolus labelled in Fig. 5.7, by plotting the streamlines near the end of inspiration coloured by the velocity magnitude. This particular alveolus is highlighted because it is oriented such that the air flows tangentially. A recirculatory centre occurs in the diseased cases but is absent in the healthy

case. As recirculating flows possess stagnation points that result in irreversible paths of massless particles [9, 38], the onset of recirculatory flow has a significant influence on the transport into the alveoli. In literature, the onset of recirculatory flow in the alveoli is determined based on the ratio of the flow rate into the alveolus (Q_a) and the flow rate through the duct (Q_d). (Q_d) is termed the shear flow [9, 43]. Quasi-steady recirculatory centres like those noted in the diseased cases in Fig. 5.9 occur for relatively small Q_a/Q_d ratios, which typically occur in the more proximal and medial generations of the acinar tree [10]. In the more distal generations, this ratio increases and the flow patterns gradually become more radial, resembling the healthy case in Fig. 5.9. In addition, literature has found that including wall motion into the numerical simulations increases the relative radial velocity component, resulting in more radial flow patterns [9].

From the above considerations, the following deductions can be made regarding Fig. 5.9. In the healthy case, the radial flow magnitude is relatively strong due to the presence of the relatively larger airway wall motion and thus recirculation is not observed. In the diseased cases, two simultaneous effects are present. The removal of alveolar septa results in a decrease in flow resistance within the duct and a concomitant increase in the shear flow component within the alveolus. Additionally, the weakening of wall motion causes a reduction in radial airflow into the alveoli. The combination of these two effects results in the noted formation of recirculatory centres in the alveolus of the diseased cases. The acinar flow field is an important factor in describing the transport of aerosols and fine particulate matter. Therefore, these changes in the flow-field will have a considerable impact on

the fates of particles inhaled into diseased lungs, considered in the following section.

5.3 Particle transport

5.3.1 Simulation conditions and boundary conditions

In order to characterize the deposition of particles in healthy and emphysematous geometries, the deposition fraction (f) quantity is defined as follows

$$f = \frac{(total\ number\ of\ particles\ deposited)}{(total\ number\ of\ particles\ released\ into\ the\ duct)} \tag{5.2}$$

In the context of this thesis a particle is assumed to have been deposited when its path intersects the wall of the computational domain. In order to characterize the spatial variation of particle deposition within the duct, the deposition fraction is computed separately for each duct. The resulting values are plotted against the normalised breath cycle τ for the cases of advancing emphysema, described in the previous section. The simulations are conducted for two particle sizes with diameters of 1 and 3 μm. These sizes represent the diameter range where particles in acinar flows are affected by a combination of the flow-field and gravity. Particles smaller than 1 μm are primarily affected by diffusive forces within the flow (e.g. Brownian motion) while particles larger than 3 μm in the acinus have their fates wholly determined by the orientation of the gravitational vector [11].

The simulations are also conducted for two separate orientations of the

Table 5.1: Simulation matrix for particle deposition study

	1 μm	3 μm	1 μm	3 μm
Healthy	Normal	Normal	Tangential	Tangential
Case I	Normal	Normal	Tangential	Tangential
Case II	Normal	Normal	Tangential	Tangential
Case III	Normal	Normal	Tangential	Tangential

gravitational vector relative to the incoming airflow into the computational domain. This is done to study the relative importance of the orientation of gravitational vector versus the airflow on the particle trajectories. One orientation is normally directed co-axially with the inflow boundary of Duct 1, while the second is directed tangentially to the same space. The particle transport simulations are conducted for the four cases (Healthy, Case I, Case II and Case III) presented in earlier chapters. For presentation purposes, the results are grouped into four categories according to particle size and orientation of the gravity vector: 1 μm Normal, 3 μm Normal, 1 μm Tangential and 3 μm Tangential. This is shown in a graphical format in Table 5.1 as a simulation matrix. The simulations are conducted for five successive breath cycles while the particle trajectories and the deposition fractions were monitored at the end of each cycle.

5.3.2 Temporal variation of deposition fraction

Figures 5.11-5.14 plot the deposition fraction for Ducts 1, 2 and 3 against the normalised respiratory breath period τ. In general, these plots of f vs τ follow a similar pattern in which the majority of the deposition occurs in the first few breath-cycles, after which f achieves a steady state value. Beyond this point, most of the particles in the domain have deposited, and

Figure 5.10: Orientation of the gravity vector with respect to the computational geometry for the normal and tangential cases respectively

the balance having been convected out of the computational domain.

From Figures 5.11-5.14 it is observed that for all cases, the greatest values of f were in Duct I, indicating that a majority of particles deposit in proximal generations of the acinus. These values of f in Duct I increase with advancing emphysema across all particle sizes and gravity vector orientations. Although Identical values of f are observed in Ducts II and III in a majority of the cases, a notable exception to this exists in scenarios which have emphysematous destruction corresponding to Case II. This Case is unique in that it is the only arrangement where the geometry is non-symmetrical about the principal axis of the model. Thus, while Duct II and III are in the same generation, only Duct II has emphysematous destruction while Duct III does not. It is observed that for all scenarios, at the Case II level, the values of f are consistently greater in Duct II than in Duct III.

As expected, particle size plays an important role in determining deposition patterns. By comparing Fig. 5.11 and 5.12 it is clear that the 3 μm particles deposit completely within one breath cycle, while 1 μm particles remain in suspension longer with their f values stabilizing around 2-2.5

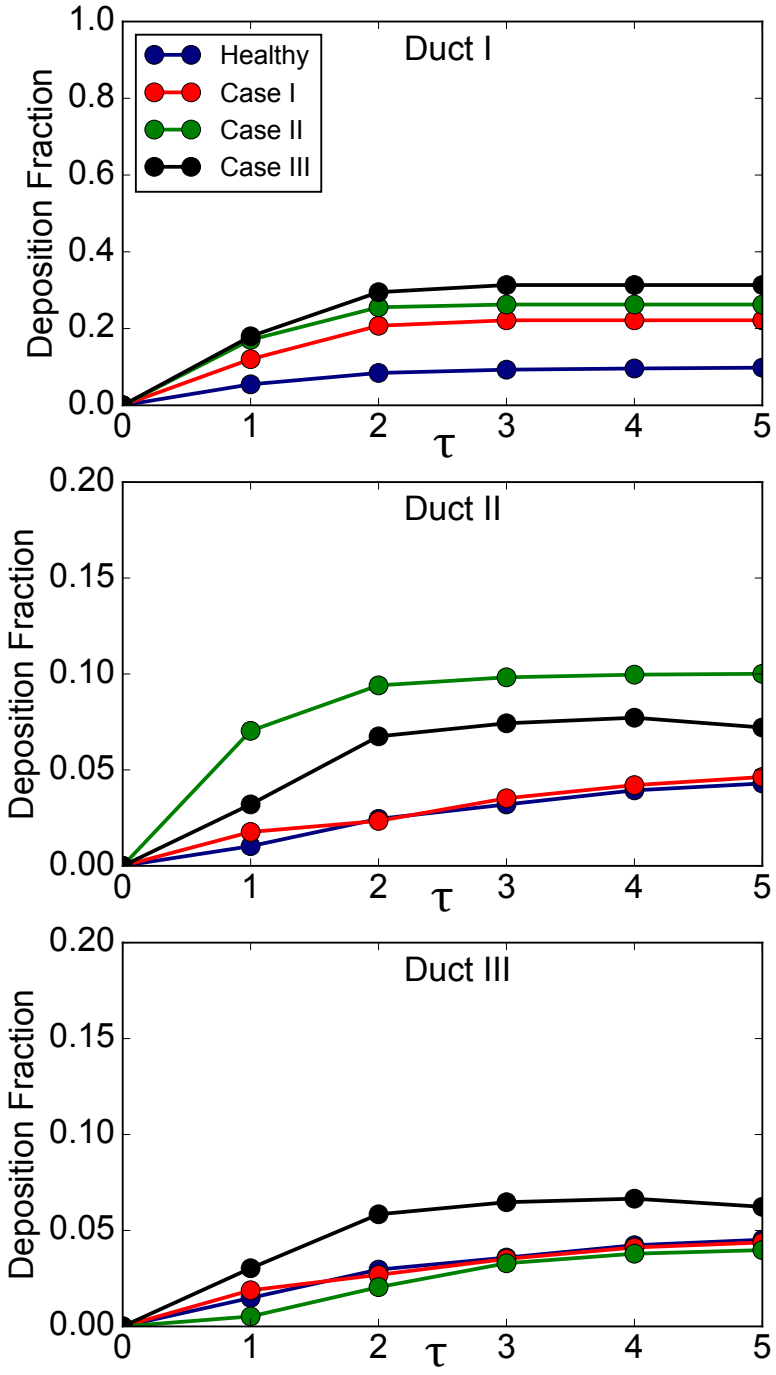

Figure 5.11: Deposition fraction of 1 μm particles, with the gravity vector oriented in the normal direction

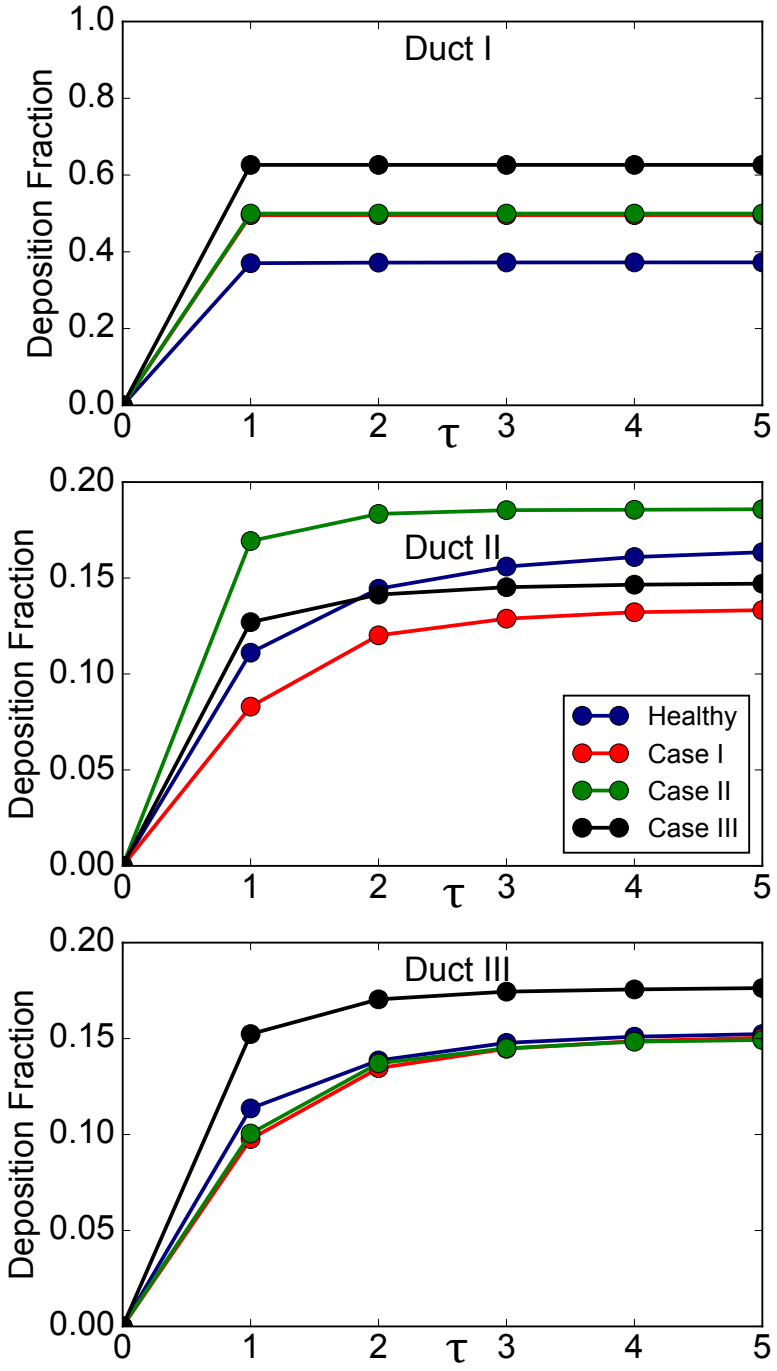

Figure 5.12: Deposition fraction of 3 μm particles, with the gravity vector oriented in the normal direction

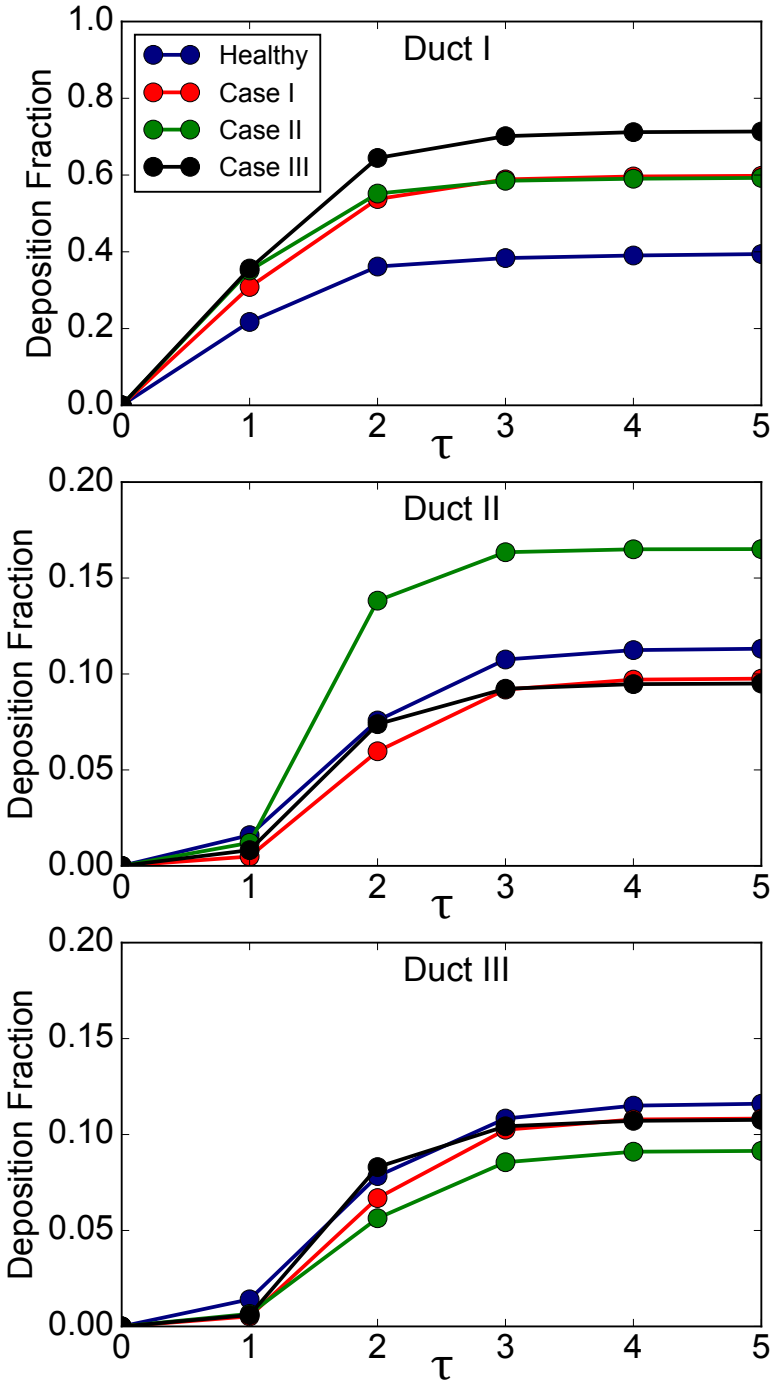

Figure 5.13: Deposition fraction of 1 μm particles, with the gravity vector oriented in the tangential direction

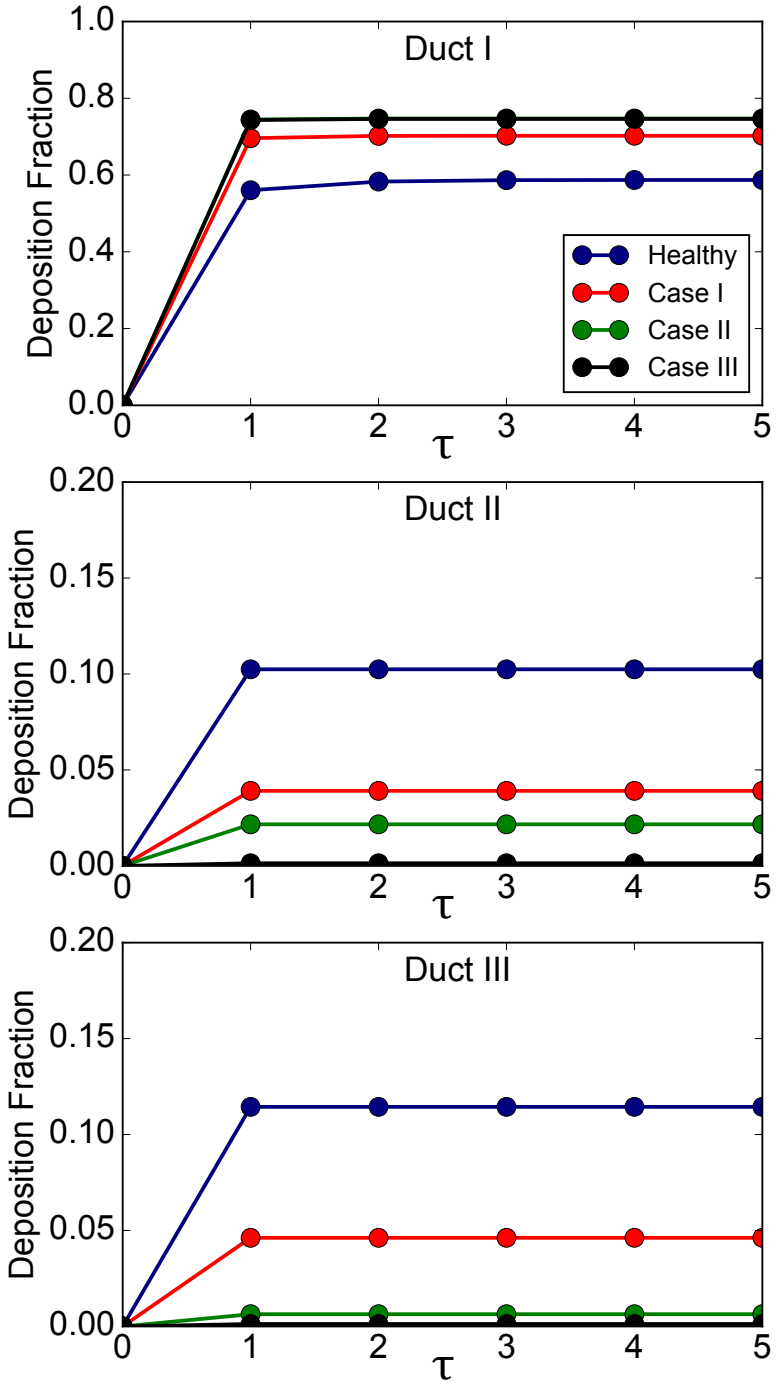

Figure 5.14: Deposition fraction of 3 μm particles, with the gravity vector oriented in the tangential direction

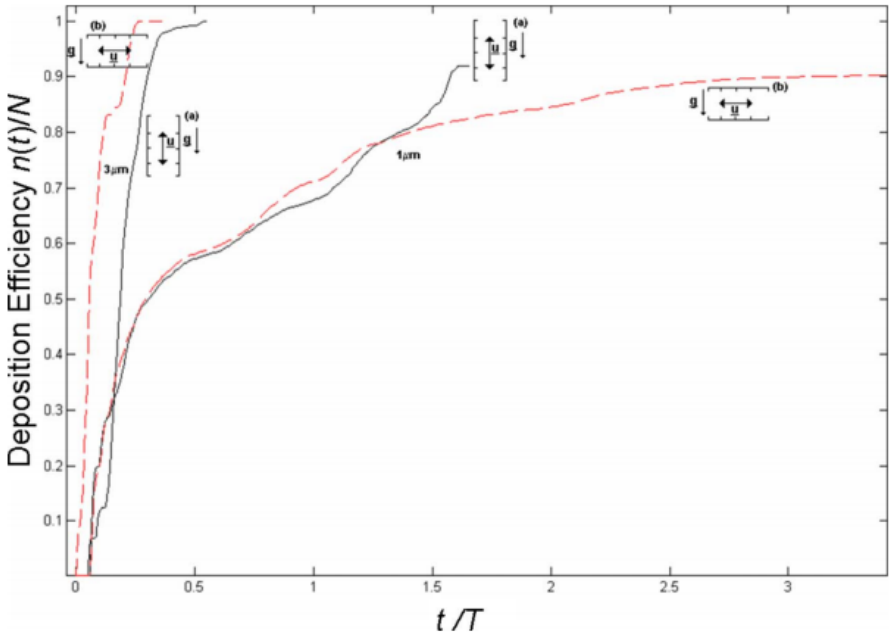

Figure 5.15: Particle deposition efficiencies under differing gravitational orientations (Adapted with permission from [11])

breath cycles. Cases with 3 μm particles are also observed to have a higher steady-state f value than their corresponding 1 μm particle cases.

The role of the orientation of the gravity vector is also significant. The cases with the gravitational vector oriented normally to the incoming flow (Figs. 5.11 and 5.12) show a greater value of f in Ducts 2 and 3 than for the corresponding tangential cases (Figs. 5.13 and 5.14).

Figures 5.11 - 5.14 also conform closely to previous simulations conducted by Sznitman et. al. [11] which have been reproduced here in Fig 5.15. While the deposition fractions for both particle sizes obtained by Sznitman et. al. are much higher, this can be explained bue to differences in geometry and boundary conditions. The Sznitman et. al. simulations tracked the deposi-

tion fraction in the third generation of the acinus and with a higher initial velocity in the boundary conditions. In the presently conducted simulation the deposition fraction was tracked in ducts lower in the acinar generational tree with differing geometry and boundary conditions.

5.3.3 Variation of steady state deposition fraction

Plots showing the variation in steady-state deposition fraction in the three ducts, for all of the simulated cases are shown in Figs. 5.16-5.19. These plots may be interpreted by keeping in mind the two competing forces of convective flow and gravity as given by Equation 2.3. The convective force and gravity reinforce each other when they are aligned as in the normal cases. In the tangential cases the gravity vector is perpendicular to the bulk incoming flow, thus directing part of it towards the acinar walls. This effect is magnified in the emphysematous cases where the convective flow is reduced.

1 μm Normal

From Fig 5.16, it is immediately apparent that for the 1 μm particles with a normal gravity vector the steady-state deposition fraction in Duct I increases with increasing levels of emphysema. While the normal case shows a f value of only 0.15, this increases in Case III to 0.32. The deposition fraction values also increase uniformly in Ducts II and III for the healthy, Case I and Case III simulations. In Case II it is observed that Duct II has a higher steady state deposition fraction (0.1) than Duct III (0.05). Since in Case II, Duct II has septal degradation while Duct III does not, this leads

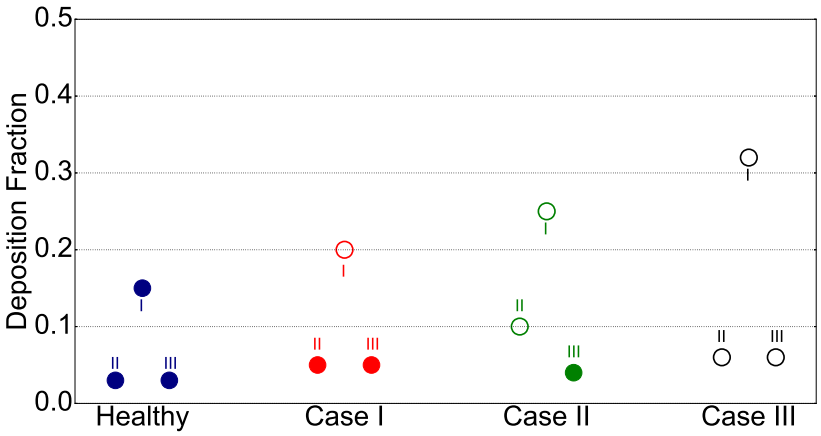

Figure 5.16: Plot of final deposition fraction after five breath cycles for 1 μm particles, gravity vector in normal direction. The filled circles indicate healthy acinar duct while empty circles indicate emphysematous destruction. The labels indicate the duct number.

to the conclusion that septal degradation preferentially enhances particulate deposition between two ducts of the same generation.

3 μm Normal

Fig 5.17 shows steady state deposition fraction values for 3 μm particles with the gravity vector oriented in the normal direction. While the steady state f in Duct I increase with advancing emphysema as with the 1 μm particle cases, it should be noted that they are much higher than the corresponding cases. The Healthy case has a steady state deposition fraction value of 0.3 while the corresponding value for Case III is 0.6. This may be attributed to the greater effect of gravity on the larger and hence heavier particles. It should also be noted that a greater proportion of particles deposit in Duct I than Ducts II and III for the diseased cases, than for the

corresponding simulations with 1 μm particles. In fact, the deposition in the proximal duct is so greatly enhanced, that the more distal Ducts II and III have lower deposition fraction values than the ones corresponding to the Healthy case under identical simulation conditions. It should also be noted that the increase in deposition fraction for Duct I is not uniform as in the 1 μm case. In particular Case I and Case II have very similar steady state values of f for Duct I (0.51 and 0.52 respectively). This may be attributed to the fact that in Case II. while the deposition is increased due to emphysematous degradation, the normal direction of the gravity vector -collinear to the incoming flow- and its increased effects due to the larger particle size direct it away from the walls and eventually deeper into the acinus. Thus lowering the deposition fraction in Duct I making it almost comparable to Case I. Case III does show an increase in deposition fraction for Duct I as compared to Case I and II. This may be attributed to a further lowering of the flow rate, which prevents the particles from being convected into the more distal generations and deposits them at the branching point between Ducts I, II and III. It should also be noted that Duct II for Case II shows greater deposition than Duct III for the same case as was observed in the previous subsection.

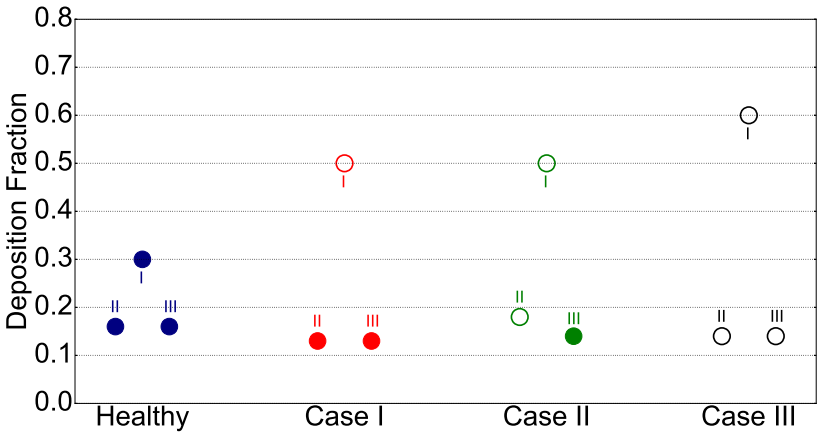

Figure 5.17: Plot of final deposition fraction after five breath cycles for 3 μm particles, gravity vector in normal direction. The filled circles indicate healthy acinar duct while empty circles indicate emphysematous destruction. labels indicate the duct number.

1 μm Tangential

Fig. 5.18 shows the steady state f values for 1 μm particles with the gravity vector oriented in the tangential direction. On comparing with the simulations with an identical particle size but a normal gravity vector, it is seen that the deposition fraction values in Duct I are consistently greater for the present cases. This is explained by the fact that the tangential gravity vector directs the particles towards the walls of the acinus instead of along the bulk flow, thereby enhancing the effects of emphysematous destruction. This also leads to a decrease in deposition fraction in the more distal ducts as compared to the healthy case. The pattern of increased deposition in Duct II as compared to Duct III in Case II is also observed here.

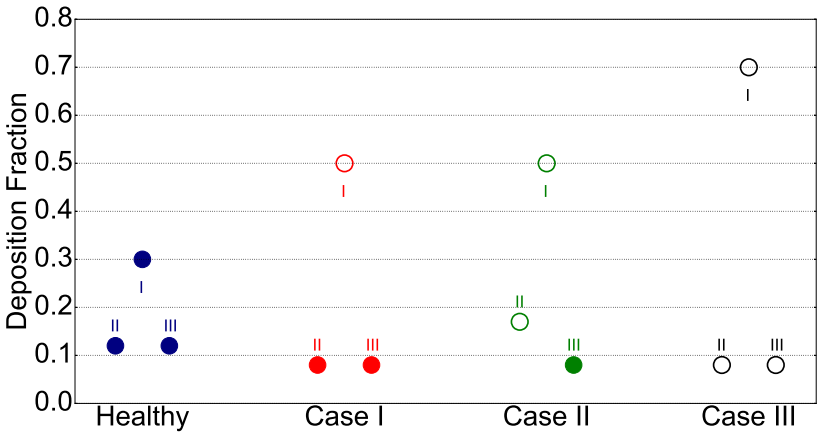

Figure 5.18: Plot of final deposition fraction after five breath cycles for 1 μm particles, gravity vector in tangential direction. The filled circles indicate healthy acinar duct while empty circles indicate emphysematous destruction. labels indicate the duct number.

3 μm Tangential

Fig. 5.19 shows the steady state f values for 3 μm particles with the gravity vector oriented in the tangential direction. These cases show the highest deposition fraction of all the cases due to the twin effects of a large particle size increasing the effect of the gravitational vector and the tangential direction of the vector that enhances deposition on the walls away from the bulk flow. There's a marked increase in deposition faction values between the Healthy case and Case III (0.5 and 0.75 respectively). However there is very little increase in deposition fraction values for Cases I, II and III. This is because the gravitational effects completely overwhelm the convective effects and since the geometrical conditions in Duct I are the same for Case I, II and III, they have identical deposition fraction values. The

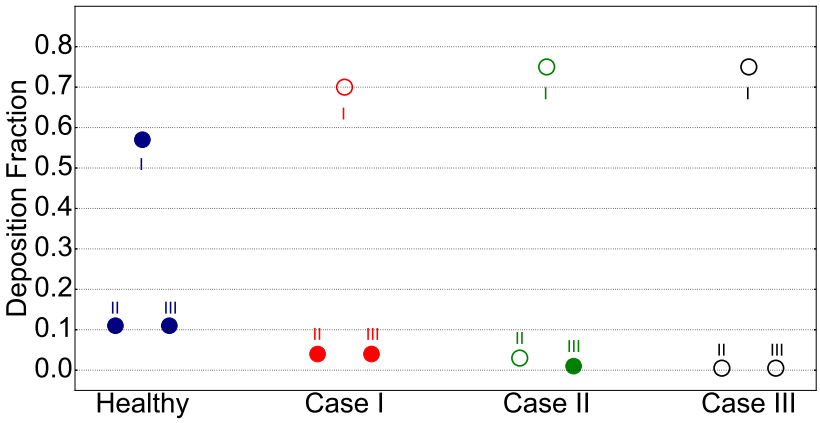

Figure 5.19: Plot of final deposition fraction after five breath cycles for 3 μm particles, gravity vector in tangential direction. The filled circles indicate healthy acinar duct while empty circles indicate emphysematous destruction. labels indicate the duct number.

pattern of increased deposition in Duct II as compared to Duct III in Case II is also observed here.

The results presented in this section particularly with reference to the increased deposition of particles within the emphysematous ducts follow closely with the results presented by Oakes et. al. [67]. However, there is considerable debate on this point as a more recent study [60] shows that the deposition in emphysematous geometries in enhanced in the healthy portions of a diseased model. This difference between experimental and numerical simulations requires further investigation and it is proposed that larger models of the complete acinus incorporating the progressive nature of emphysema as has been presented here might help to discover the mechanism responsible for enhancement or diminishment of particle deposition in emphysematous models.

Chapter 6

Summary and Conclusions

6.1 Model development

A CFD model has been developed, to simulate the effects of COPD, specifically early-stage emphysema in the airways of the pulmonary acinus. The airway structure was based on a mathematical model developed by Fung [7], using a 14-hedrons geometry to provide a close packed alveoli structure surrounding a central duct was achieved by the arrangement of 14-hedrons. The computational geometry consisted of two generations - the fourth and fifth- of the acinus. The fourth generation consisted of a single duct (Duct 1) which branched into two identical ducts (Ducts 2 and 3) that formed the fifth generation. During inspiration, the incoming air entered via a single entryway into Duct 1 and exited through Ducts 2 and 3 each of which had two exits. During expiration this process was reversed. The computational domain underwent a self-similar time-dependent sinusoidal motion of expansion and contraction, which was implemented in order to simulate the real-world motion of airways that provides the pressure differential that is responsible for the inspiratory and expiratory airflow. The boundary conditions in the model were adjusted so as to mimic the appropriate air-flow rates. The effects of emphysema were incorporated by two methods. The

emphysematous destruction of parenchymal tissue was modelled as septal degradation in the ducts. The progressive nature of the disease was also incorporated with the inclusion of successive cases where the septal destruction was present in one, two and three of the ducts in the domain. The loss of the parenchymal mesh that normally provides the elastic recoil necessary for the proper functioning of the airways was also incorporated into the disease model by changing the amplitude of sinusoidal motion of the airway domain. This measure is also complemented by a corresponding loss in flow-rate that is observed under actual physiological conditions.

6.2 Oxygen transport and flow-field

The oxygen transport through the computational domain was tracked by solving a scalar transport diffusion equation. A parameter $\overline{C}$ was defined in order to quantify the change in concentration of oxygen over a single inhalation. Tracking this parameter over the different, progressive cases of emphysema, it was observed that increasing levels of emphysema corresponded to a decrease in the parameter across all three ducts. It was further observed that this behavior was mainly caused by a decrease in airway wall motion and the corresponding loss in flow rate rather than the septal degradation. This is readily explained by the fact that while the majority of the gaseous transport occurs by diffusion rather than advection, the loss in airflow rate due to disease is sufficient enough to decrease the oxygen levels by almost 5 % in the most extreme cases.

The effect of the disease on the flow-field was quantified through the

static pressure-drop across each of the ducts for the different cases. It was observed that both the septal destruction and the decrease in airway wall motion and its attendant loss in flow-rate both led to an overall static pressure drop. However, the airflow was preferentially increased through those regions which had septal destruction. While this may seem to indicate that acinar generations with septal destruction might be better ventilated than their healthy counterparts, it should be remembered that septal destruction is usually accompanied by a loss in static pressure recoil which decreases the available pressure driving the breath-cycle resulting in an overall decrease in flow-rate and consequently poorer ventilation.

The diseased conditions were also observed to have a direct impact on the temporal dynamics of the flow-field over a single breath cycle. While re-circulatory flow motions are usually observed in acinar generations proximal to those included in this simulation (up to the 3rd generation of the acinus), it was noted that with the inclusion of the effects of emphysema, a recirculatory centre developed at the proximal end of the alveolus during inspiration, which increased in intensity in proportion to the extent of the disease.

6.3 Particle transport

In order to study the effects of the disease on particle transport into the lung, simulations were conducted using two different particle sizes (1 μm and 3 μm). At these sizes the principal forces affecting the particles are convective forces due to the flow and gravitational force. As a result, two

sets of simulations were conducted with the gravity vector being oriented in a direction normal and tangential to the flow at the domain entrance respectively. Particle deposition was quantified by the particle deposition fraction which was the number of particles deposited divided by the total number introduced into the domain during the initial inspiration. The particle deposition fraction was tracked in the computational domain for a total of five consecutive breath cycles.

The results show that the deposition fraction was increased in emphysematous ducts due to both a decrease in airway wall motion, and emphysematous destruction, thereby indicating that the earliest stages of the disease enhanced depositions in the ducts. This results in in an increased risk for disease propagation. The increase in deposition fraction in ducts distal to the first emphysematous ducts depended on the particle size and orientation of the gravitational vector. Smaller particles and a gravitational vector aligned with the the flow tend to penetrate and deposit deeper into the acinus, while the larger particles and a tangential gravitational vector tended to promote the deposition of particles in the proximal ducts of the acinus. It was also observed that for two ducts in the same generation, particles would preferentially deposit in the one with emphysematous destruction as compared to one without. Thus, while emphysema notably enhanced the deposition in the first duct encountered by particles, the deposition patterns in the subsequent ducts depended on particle size, gravitational vector orientation and the presence of emphysematous destruction in the distal airways.

6.4 Summary of conclusions

- The onset of emphysema causes a significant drop in oxygen transport within the acinus.
- This loss of oxygen transported to the acinus during inhalation is primarily due to the loss in elastic recoil which causes a related drop in incoming airflow rate.
- Emphysema causes a drop in hydraulic losses within the acinus with the flow resistance dropping appreciably in ducts affected by septal destruction.
- The effects of emphysema changes the flow field within the alveolar cavity with the appearance of a recirculatory centre with the alveoli in the diseased cases indicating an increase in shear flow and decrease in flow into the alveolar cavity.
- While particle size and the orientation of the gravitational vector play an important part in deposition within the acinus, emphysematous destruction increases the particle deposition in any duct across all particle sizes and orientations. This is due to both the decrease in airway wall motion and emphysematous septal destruction.
- For two ducts in the same alveolar generation, the duct with septal destruction shows greater deposition regardless of particle size or gravitational vector orientation.
- Smaller particles with a gravity vector oriented coaxially to the incom-

ing flow allow particles to penetrate and deposit deep in the acinus, while larger particles with other gravitational orientations tend to deposit in more proximal generations

6.5 Future work

While this study was successful in implementing a model of emphysema and applying to an isolated section of the pulmonary acinus, it should be noted that the complete structure of the airway tree is extremely heterogeneous. As a result, reliable predictions of the effects of emphysema on the factors investigated in this study over multiple airway generations will require the development of a larger computational domain spanning the entire pulmonary acinus or even perhaps multiple acini. Incorporation of realistic patient data to set appropriate flow rate boundary conditions for varying stages of emphysema is also an additional refinement that should be considered. In short, therefore, future works along these lines must incorporate multiple airway generations and a larger number of cases with varying levels of emphysema, in order to make accurate predictions of the effects of a disease that affects the extremely heterogeneous human pulmonary airway system.

Bibliography

[1] C Kleinstreuer and Z Zhang. Airflow and Particle Transport in the Human Respiratory System. *Annual Review of Fluid Mechanics*, 42(1): 301–334, 2010. → pages xi, 3, 11, 21

[2] W Mitzner. Emphysema A Disease of Small Airways or Lung Parenchyma? *New England Journal of Medicine*, 365(17):1637–1639, 2011. → pages xi, 7

[3] ER Weibel, B Sapoval, and M Filoche. Design of Peripheral Airways for Efficient Gas Exchange. *Respiratory physiology & neurobiology*, 148 (1):3–21, 2005. → pages xi, xii, 12, 19

[4] DL Fry and RE Hyatt. Pulmonary Mechanics* A Unified Analysis of the Relationship Between Pressure, Volume and Gas Flow in the Lungs of Normal and Diseased Human Subjects. *The American Journal of Medicine*, 29, 1960. → pages xi, 13

[5] JB West. *Pulmonary Pathophysiology : The Essentials*. Lippincott Williams and Wilkins, 2005. → pages xi, 7, 14, 16, 44

[6] ER Weibel, AF Cournand, and DW Richards. *Morphometry of the*

Human Lung With a Foreword. Springer Berlin Heidelberg, 1963. → pages xii, 10, 11, 17, 19

[7] Y C Fung. A Model of the Lung Structure and its Validation. *Journal of Applied Physiology*, 1988. → pages xii, 20, 21, 28, 36, 85

[8] H Kumar, MH Tawhai, EA Hoffman, and CL Lin. The Effects of Geometry on Airflow in the Acinar Region of the Human Lung. *Journal of Biomechanics*, 42:1635–1642, 2009. → pages xii, 20, 24, 25, 36, 69

[9] A Tsuda, FS Henry, and JP Butler. Chaotic Mixing of Alveolated Duct Flow in Rhythmically Expanding Pulmonary Acinus. *Journal of Applied Physiology*, 1995. → pages xii, 19, 24, 25, 70

[10] P Hofemeier, R Fishler, and J Sznitman. The role of respiratory flow asynchrony on convective mixing in the pulmonary acinus. *Fluid Dynamics Research*, 46(4):041407, 2014. → pages xii, 26, 36, 70

[11] J Sznitman, T Heimsch, JH Wildhaber, A Tsuda, and T Rösgen. Respiratory Flow Phenomena and Gravitational Deposition in a Three-Dimensional Space-Filling Model of the Pulmonary Acinar Tree. *Journal of Biomechanical Engineering*, 2009. → pages xii, xv, 20, 28, 29, 30, 36, 43, 71, 78

[12] J Vestbo, SS. Hurd, AG. Agusti, PW. Jones, C Vogelmeier, A Anzueto, PJ Barnes, LM Fabbri, FJ Martinez, M Nishimura, et al. Global strategy for the diagnosis, management, and prevention of chronic obstructive pulmonary disease: Gold executive summary. *American Journal*

of Respiratory and Critical Care Medicine, 187(4):347–365, 2013. → pages 1, 2, 3, 4, 5

[13] N Mittmann, L Kuramoto, SJ Seung, JM Haddon, C Bradley-Kennedy, and JM Fitzgerald. The cost of moderate and severe copd exacerbations to the canadian healthcare system. *Respiratory Medicine*, 102(3):413–421, 2008. → pages 1

[14] SD Shapiro. The pathogenesis of emphysema: The elastase antielastase hypothesis 30 years later. *Proceedings of the Association of American Physicians*, 107(3):346–352, 1995. → pages 3

[15] JL Wright and A Churg. Advances in the Pathology of COPD. *Histopathology*, 49(1):1–9, jul 2006. → pages 3

[16] DM Mannino, AS Buist, TL Petty, PL Enright, and SC Redd. Lung function and mortality in the united states: Data from the first national health and nutrition examination survey follow up study. *Thorax*, 58 (5):388–393, 2003. → pages 4

[17] JC Hogg and S Van Eeden. Pulmonary and systemic response to atmospheric pollution. *Respirology*, 14(3):336–346, 2009. → pages 4

[18] P Lee, TR Gildea, and JK Stoller. Emphysema in nonsmokers: Alpha 1-antitrypsin deficiency and other causes. *Cleveland Clinic Journal of Medicine*, 69(12):928–9, 2002. → pages 4

[19] NA Zwar, GB Marks, O Hermiz, S Middleton, EJ Comino, I Hasan, S Vagholkar, and SF Wilson. Predictors of accuracy of diagnosis of

chronic obstructive pulmonary disease in general practice. *Medical Journal of Australia*, 195(4):168–71, 2011. → pages 4

[20] TMA Wilkinson, GC Donaldson, JR Hurst, TAR Seemungal, and JA Wedzicha. Early therapy improves outcomes of exacerbations of chronic obstructive pulmonary disease. *American Journal of Respiratory and Critical Care Medicine*, 169(12):1298–1303, 2004. → pages 5

[21] DB Coultas, D Mapel, R Gagnon, and EVA Lydick. The Health Impact of Undiagnosed Airflow Obstruction in a National Sample of United States Adults. *American Journal of Respiratory and Critical Care Medicine*, 164(3):372–377, aug 2001. → pages 5

[22] S Leung, AE Gallagher, V Kvetan, and LA Eisen. Barriers to Ultrasonography Training in Critical Care Medicine Fellowships: A Survey of Program Directors. *Chest*, 136(4 MeetingAbstracts):49S–50S, 2009. doi: 10.1378/chest.09-0553. → pages 6

[23] R Pellegrino, G Viegi, V Brusasco, RO Crapo, F Burgos, R Casaburi, A Coates, CPM Van Der Grinten, P Gustafsson, J Hankinson, R Jensen, DC Johnson, N MacIntyre, R McKay, MR Miller, D Navajas, OF Pedersen, and J Wanger. Interpretative Strategies for Lung Function Tests. *European Respiratory Journal*, 26(5):948–968, 2005. → pages 6

[24] WM Thurlbeck. *Chronic Airflow Obstruction in Lung Disease*. WB Saunders Company, 1976. → pages 6

[25] GL Snider. Emphysema: The First Two Centuries-and Beyond. A Historical Overview, With Suggestions of Future Research: Part 2. *American Review of Respiratory Disease*, 146(6):1615–22, 1992. → pages 6

[26] GL Snider, J Kleinerman, WM Thurlbeck, and ZH Bengali. The Definition of Emphysema. *American Review of Respiratory Disease*, 132 (1):182–185, jul 1985. → pages 6

[27] Stephen Milne and Gregory G King. Advanced imaging in copd: insights into pulmonary pathophysiology. *Journal of thoracic disease*, 6 (11):1570, 2014. → pages 8

[28] Julia Ley-Zaporozhan, Sebastian Ley, and Hans-Ulrich Kauczor. Morphological and functional imaging in copd with ct and mri: present and future. *European Radiology*, 18(3):510–521, 2008. → pages 8

[29] D Aykac, EA Hoffman, G Mclennan, and JM Reinhardt. Segmentation and Analysis of the Human Airway Tree from Three-Dimensional X-ray CT Images. *IEEE Transactions on Medical Imaging*, 22(8):940–950, Aug 2003. → pages 10

[30] K Horsfield and G Cumming. Morphology of the bronchial tree in man. *Journal of Applied Physiology*, 24(3):373–383, 1968. → pages 10

[31] Design of Peripheral Airways for Efficient Gas Exchange. In *Respiratory Physiology and Neurobiology*, 2005. → pages 10

[32] B Haefeli-Bleuer and ER Weibel. Morphometry of the Human Pul-

monary Acinus. *The Anatomical Record*, 220(4):401–414, 1988. → pages 11, 17, 23

[33] ER Weibel. *The Pathway for Oxygen*. Harvard University Press, 1984. → pages 12

[34] JH Mateika and J Duffin. A Review of the Control of Breathing During Exercise. *European Journal Applied Physiology*, 71:1–27, 1995. → pages 12, 13

[35] DE O'donnell and P Laveneziana. Physiology and consequences of lung hyperinflation in copd. *European Respiratory Review*, 15(100):61–67, 2006. → pages 14

[36] RE Hyatt. Expiratory flow limitation. *Journal of Applied Physiology*, 55(1):1–7, 1983. → pages 14

[37] SV Dawson and EA Elliott. Wave-speed limitation on expiratory flow-a unifying concept. *Journal of Applied Physiology*, 43(3):498–515, 1977. → pages 14

[38] FS Henry, JP Butler, and A Tsuda. Kinematically Irreversible Acinar Flow: A Departure from Classical Dispersive Aerosol Transport Theories. *Journal of Applied Physiology*, 92(2):835–845, 2002. → pages 19, 25, 70

[39] J Sznitman, F Heimsch, T Heimsch, D Rusch, and T Rösgen. Three-Dimensional Convective Alveolar Flow Induced by Rhythmic Breathing

Motion of the Pulmonary Acinus. *Journal of Biomechanical Engineering*, 2007. → pages 19, 24, 25, 41, 43, 69

[40] A Tsuda, JP Butler, and JJ Fredberg. Effects of Alveolated Duct Structure on Aerosol Kinetics II. Gravitational Sedimentation and Inertial Impaction. *Journal of Applied Physiology*, 76(6):2510–2516, 1994. → pages 20, 23

[41] P Hofemeier and J Sznitman. Role of alveolar topology on acinar flows and convective mixing. *Journal of Biomechanical Engineering*, 136(6): 061007, 2014. → pages 20, 36

[42] TJ Pedley. Pulmonary Fluid Dynamics. *Annual Review of Fluid Mechanics*, 9(1):229–274, 1977. → pages 21

[43] J Sznitman. Respiratory Microflows in the Pulmonary Acinus. *Journal of Biomechanics*, 46:284–298, 2013. → pages 21, 22, 23, 26, 36, 70

[44] CD Murray. The Physiological Principle of Minimum Work: I. The Vascular System and the Cost of Blood Volume. *Proceedings of the National Academy of Sciences of the United States of America*, 12(3): 207–214, 1926. → pages 23

[45] MR Davidson and JM Fitz-Gerald. Flow Patterns in Models of Small Airway Units of the Lung. *Journal of Fluid Mechanics*, 52(01):161–177, 1972. → pages 23

[46] HK Chang, RT Cheng, and LE Farhi. A Model Study of Gas Diffusion

in Alveolar Sacs. *Respiration Physiology*, (18):386–397, 1973. → pages 23

[47] WJ Federspiel and JJ Fredberg. Axial Dispersion in Respiratory Bronchioles and Alveolar Ducts. *Journal of Applied Physiology*, 64(6):2614–2621, 1988. → pages 23

[48] CP Yu and S Rajaram. Diffusional Deposition of Particles in a Model Alveolus. *Journal of Aerosol Science*, 9(6):521–525, 1978. → pages 23

[49] C Darquenne and M Paiva. Two- and Three-Dimensional Simulations of Aerosol Transport and Deposition in Alveolar Zone of Human Lung. *Journal of Applied Physiology*, 80(4):1401–1414, apr 1996. → pages 23, 24

[50] C Darquenne. A Realistic Two-Dimensional Model of Aerosol Transport and Deposition in the Alveolar Zone of the Human Lung. *Journal of Aerosol Science*, 32(10):1161–1174, 2001. → pages 23

[51] M Horner, G Metcalfe, S Wiggins, and JM Ottino. Transport Enhancement Mechanisms in Open Cavities. *Journal of Fluid Mechanics*, 452: 199–229, 2002. → pages 24

[52] B Ma, V Ruwet, P Corieri, R Theunissen, M Riethmuller, and C Darquenne. CFD Simulation and Experimental Validation of Fluid Flow and Particle Transport in a Model of Alveolated Airways. *Journal of Aerosol Science*, 40(5):403–414, 2009. → pages 24

[53] JM Ottino. *The Kinematics of Mixing: Stretching, Chaos, and Transport*, volume 3. Cambridge university press, 1989. → pages 24

[54] PD Anderson, OS Galaktionov, GWM Peters, FN Van de Vosse, and HEH Meijer. Analysis of Mixing in Three-Dimensional Time-Periodic Cavity Flows. *Journal of Fluid Mechanics*, 386:149–166, 1999. → pages 24

[55] WH Finlay. *The Mechanics of Inhaled Pharmaceutical Aerosols: an Introduction*. Academic Press, 2001. → pages 27

[56] A Tsuda, FS Henry, and JP Butler. Particle Transport and Deposition: Basic Physics of Particle Kinetics. *Comprehensive Physiology*, 3(4): 1437–1471, 2013. → pages 27

[57] JM Oakes, AL Marsden, C Grandmont, S C Shadden, C Darquenne, and IE Vignon-Clementel. Airflow and particle deposition simulations in health and emphysema: From in vivo to in silico animal experiments. *Annals of Biomedical Engineering*, 42(4):899–914, 2014. → pages 31

[58] EJ Berg. Stereoscopic particle image velocimetry analysis of healthy and emphysemic acinus models. *Journal of Biomechanical Engineering*, 2010. → pages 31

[59] P Aghasafari, IBM Ibrahim, and RM Pidaparti. Investigation of the effects of emphysema and influenza on alveolar sacs closure through cfd simulation. *Journal of Biomedical Science and Engineering*, 9(06):287, 2016. → pages 31

[60] Jessica M. Oakes, Philipp Hofemeier, Irene E. Vignon-Clementel, and Josué Sznitman. Aerosols in healthy and emphysematous in silico pulmonary acinar rat models. *Journal of Biomechanics*, 49(11):2213–2220, 2015. → pages 31, 84

[61] Bernard Sapoval, M Filoche, and ER Weibel. Smaller is betterbut not too small: a physical scale for the design of the mammalian pulmonary acinus. *Proceedings of the National Academy of Sciences*, 99(16):10411–10416, 2002. → pages 43

[62] Philipp Hofemeier, Lihi Shachar-Berman, Janna Tenenbaum-Katan, Marcel Filoche, and Josué Sznitman. Unsteady diffusional screening in 3d pulmonary acinar structures: from infancy to adulthood. *Journal of biomechanics*, 2015. → pages 43

[63] J Sznitman. Convective gas transport in the acinus: revisiting the role of effective diffusivity. In *6th World Congress of Biomechanics (WCB 2010). August 1-6, 2010 Singapore*, pages 370–373. Springer, 2010. → pages 44

[64] CM Rhie and WL Chow. Numerical study of the turbulent flow past an airfoil with trailing edge separation. *AIAA Journal*, 21(11):1525–1532, 1983. → pages 48

[65] S Patankar. *Numerical Heat Transfer and Fluid Flow*. CRC press, 1980. → pages 48

[66] PD Wagner, DR Dantzker, R Dueck, JL Clausen, and JB West. Ventilation-Perfusion Inequality in Chronic Obstructive Pulmonary

Disease. *The Journal of Clinical Investigation*, 59:203–216, 1977. → pages 56

[67] Jessica M. Oakes, Alison L. Marsden, Cline Grandmont, Chantal Darquenne, and Irene E. Vignon-Clementel. Distribution of aerosolized particles in healthy and emphysematous rat lungs: Comparison between experimental and numerical studies. *Journal of Biomechanics*, 48(6):1147 – 1157, 2015. → pages 84

Appendix

Fluent Mesh Motion UDF

The mesh motion that simulates the rhythmic movement of pulmonary airways is implemented in Fluent by the use of a User Defined Function (UDF). The function is written in a heavily templatted version of C++ and implements Eqtn. 4.4 over all points in the computational domain.

```
#include "udf.h"
#include "unsteady.h"
#include "mem.h"
FILE *fout;
/* &&&&&&&&&&&&&&&&&&&&&&&&&&&&&&&&&&&&&&&&&&&&&&&&&&&&&&&&&&&&&& */
DEFINE_ON_DEMAND(save_original_grid_to_nodes)
{
#if !RP_HOST
   save_original_grid_to_nodes_func();
   Message0("\n\n Done! \n  You can check this through plotting the
       contours of user defined node memory (e.g. print on
       walls)\n");
#endif /*!RP_HOST */
}

void save_original_grid_to_nodes_func()
{
   Domain *domain;
   cell_t c;
   Thread *t;
   Node *v;
   int n;
   domain=Get_Domain(1);
   /*Store the mesh node coordinates in user-defined node memory,
       this data is used in the dynamic mesh*/
   thread_loop_c (t,domain)
   {
```

```
      begin_c_loop (c,t)
      {
         c_node_loop (c,t,n)
         {
            v = C_NODE(c,t,n);
            N_UDMI(v,0) = NODE_X(v);
            N_UDMI(v,1) = NODE_Y(v);
            N_UDMI(v,2) = NODE_Z(v);
         }
      }
      end_c_loop (c,t)
   }
}
DEFINE_GRID_MOTION(Parenchyma1,domain,dt,time,dtime)
{
#if !RP_HOST
Thread *tf= DT_THREAD(dt);
face_t f;
Node *v;
real NV_VEC(A);
real NV_VEC(dx);
real previous_time;
int n;
int v1;
int i;
float beta;
/* calculate displacement vector at the node normal to the surface
    */

i=0;
begin_f_loop(f,tf)
{
previous_time=PREVIOUS_TIME;
F_AREA(A,f,tf);
beta = 0.0416;
amplitude=beta/2;

dx[0]=amplitude*(A[0]/NV_MAG(A)*waveform);
dx[1]=amplitude*(A[1]/NV_MAG(A)*waveform);
dx[2]=amplitude*(A[2]/NV_MAG(A)*waveform);
f_node_loop(f,tf,n)
 {
 v = F_NODE(f,tf,n);
 /* update node if the current node has not been previously */
 /* visited when looping through previous faces */
```

```
 if ( NODE_POS_NEED_UPDATE (v))
 {
 /* indicate that node position has been update */
 /*so that it's not updated more than once */
 NODE_POS_UPDATED(v);

NODE_COORD(v)[0]=N_UDMI(v,0)*(1.0+ amplitude +
    amplitude*sin(1.62885*CURRENT_TIME - (3.141/2)));
NODE_COORD(v)[1]=N_UDMI(v,1)*(1.0+ amplitude+
    amplitude*sin(1.62885*CURRENT_TIME - (3.141/2)));
NODE_COORD(v)[2]=N_UDMI(v,2)*(1.0+ amplitude +
    amplitude*sin(1.62885*CURRENT_TIME - (3.141/2)));

i=i+1;
 }
 }
}
 end_f_loop(f,tf);
 #endif /*!RP_HOST*/
}
/* &&&&&&&&&&&&&&&&&&&&&&&&&&&&&&&&&&&&&&&&&&&&&&&&&&&&&&&&&&&&&&&&&& */
```